J. Fluid Mech. (2011), *vol.* 677, *pp.* 305–341.
doi:10.1017/jfm.2011.85

The collapse of single bubbles and approximation of the far-field acoustic emissions for cavitation induced by shock wave lithotripsy

A. R. JAMALUDDIN[1]†, G. J. BALL[2], C. K. TURANGAN[3] AND T. G. LEIGHTON[4]‡

[1]School of Engineering Sciences, University of Southampton, Highfield SO17 1BJ, UK
[2]Atomic Weapons Establishment, Aldermaston, Reading RG7 4PR, UK
[3]Institute of High Performance Computing, Singapore 138632
[4]Institute of Sound and Vibration Research, University of Southampton, Highfield SO17 1BJ, UK

(Received 2 August 2010; revised 17 January 2011; accepted 14 February 2011; first published online 27 April 2011)

Recent clinical trials have shown the efficacy of a passive acoustic device used during shock wave lithotripsy (SWL) treatment. The device uses the far-field acoustic emissions resulting from the interaction of the therapeutic shock waves with the tissue and kidney stone to diagnose the effectiveness of each shock in contributing to stone fragmentation. This paper details simulations that supported the development of that device by extending computational fluid dynamics (CFD) simulations of the flow and near-field pressures associated with shock-induced bubble collapse to allow estimation of those far-field acoustic emissions. This is a required stage in the development of the device, because current computational resources are not sufficient to simulate the far-field emissions to ranges of $O(10\,\mathrm{cm})$ using CFD. Similarly, they are insufficient to cover the duration of the entire cavitation event, and here simulate only the first part of the interaction of the bubble with the lithotripter shock wave in order to demonstrate the methods by which the far-field acoustic emissions resulting from the interaction can be estimated. A free-Lagrange method (FLM) is used to simulate the collapse of initially stable air bubbles in water as a result of their interaction with a planar lithotripter shock. To estimate the far-field acoustic emissions from the interaction, this paper developed two numerical codes using the Kirchhoff and Ffowcs William–Hawkings (FW-H) formulations. When coupled to the FLM code, they can be used to estimate the far-field acoustic emissions of cavitation events. The limitation of the technique is that it assumes that no significant nonlinear acoustic propagation occurs outside the control surface. Methods are outlined for ameliorating this problem if, as here, computational resources cannot compute the flow field to sufficient distance, although for the clinical situation discussed, this limitation is tempered by the effect of tissue absorption, which here is incorporated through the standard derating procedure. This approach allowed identification of the sources of, and explanation of trends seen in, the characteristics of the far-field emissions observed in clinic, to an extent that was sufficient for the development of this clinical device.

Key words: bubble dynamics, cavitation, hydrodynamic noise

† Present address: Romax Technology Limited, Nottingham Science and Technology Park, Nottingham NG7 2PZ, UK
‡ Email address for correspondence: T.G.Leighton@soton.ac.uk

1. Introduction

Shock wave lithotripsy (SWL; also known as extracorporeal shock wave lithotripsy) is a technique for fragmenting kidney or gall stones with shock waves (Lingeman *et al.* 2009; Leighton & Cleveland 2010). It involves focusing thousands of shocks onto the stones to break them into small pieces that can be dissolved by drugs or passed in urine. A variety of mechanisms could potentially contribute to stone fragmentation, including direct action of stress and cavitation. Cavitation bubbles are almost certainly very important, and have been observed both *in vitro* and *in vivo* during lithotripsy (Coleman *et al.* 1987; Kuwahara *et al.* 1989; Coleman *et al.* 1992, 1993; Delius & Gambihler 1992; Zhong *et al.* 1997; Cleveland *et al.* 2000). The interaction of shock with cavitation, stone and tissue generates far-field acoustic signals that, it was suggested, could be detected by a passive acoustic device and used as an indicator of the effectiveness of the lithotripter shock in breaking the stone (Coleman *et al.* 1992, 1993; Leighton 1994, 2004; Fedele *et al.* 2004; Bailey *et al.* 2005). The requirement for such a device is clear from the fact that around 30 %–50 % of patients require re-treatment.

A recent clinical study of this new device for the efficacy of the SWL provided a test of the treatment success that has 91.7 % sensitivity automatically delivered by the device (Leighton *et al.* 2008*a*,*b*). Using state-of-the-art diagnostic suites on the same set of patient treatments in-theatre, clinicians scored a sensitivity of 36.8 %, although statistics from current clinical trials on how use of the machine affects re-treatment rates will be more meaningful. Some clinicians are exploring the extent to which the device might condense the 'patient pathway' (DH 2004) so that, for example, the signals detected in the first hundred or so shocks on a patient can be used (prior to the likely onset of adverse side effects) to predict whether it is worth continuing with lithotripsy or whether the patient should be sent instead for ureteroscopic stone removal (Smith *et al.* 2009; Fedele *et al.* 2010; Leighton & Cleveland 2010).

The simulations conducted here are to predict the far-field pressure emissions. The link between these and damage is made through empirical observation of patients (Leighton *et al.* 2008*c*), and there is no intention here of linking the calculated pressure and flow fields to damage. The search for such a direct linkage is subject to an ongoing and intensive international research effort (Philipp & Lauterborn 1998; Tong *et al.* 1999; Eisenmenger 2001; Zhong, Zhou & Zhu 2001; Zhu *et al.* 2002; Cleveland & Sapozhnikov 2005; Birkin *et al.* 2005*a*; Calvisi *et al.* 2007; Klaseboer *et al.* 2007; Sapozhnikov *et al.* 2007; Calvisi, Iloreta & Szeri 2008; Iloreta, Fung & Szeri 2008; Lauterborn & Kurz 2010). To be clinically relevant, the output of such research would require challenging extrapolation to clinical tissue from the materials used in laboratory experiments or simulations (e.g. water, stone phantoms and rigid boundaries). To enable the new device to be developed before completion of such a lengthy international research effort, in the current study the simulations were conducted in parallel with laboratory and patient experiments (Leighton *et al.* 2008*a*,*b*,*c*).

Development of this device (Leighton *et al.* 2008*c*) did not assume that cavitation was the sole source of stone fragmentation but rather designed a tool that interpreted the far-field acoustic emissions generated by the interaction of the shock, tissue, cavitation and stone. Such interpretations should be based on predictive simulations of the far-field acoustic emissions that would result from those interactions. It is important to understand the advantages and limitations of each method of simulating cavitation events. When lithotripter shock waves interact with a bubble,

sub-microsecond features are crucial, but the sequence of events can last hundreds of microseconds. The method described here brings to the range of available techniques the ability to include liquid compressibility and blast wave generation, high-speed liquid jets and loss of bubble sphericity, bubble fragmentation and (with limited geometries) multi-bubble interactions.

Current computational resources however limit the scope of practical numerical simulations to less than the first microsecond of the interaction. Earlier methods had also included loss of sphericity and jets, but not compressibility or bubble fragmentation, and operate on a similarly restricted time scale (Blake, Taib & Doherty 1986; Ding & Gracewski 1996; Blake *et al.* 1997). In contrast, the most popular method for simulating lithotripter shock–bubble interaction is through the use of the Gilmore equation, which can cover the hundreds of microseconds required to encompass the initial collapse of the bubble (simulated here), and also the subsequent expansion under the prolonged tensile portion of the lithotripter pulse, followed by the second collapse. However, the Gilmore equation can only model a single bubble and must assume spherical symmetry (so neglecting jetting and fragmentation). The Gilmore equation also assumes that the pressure field in the liquid radiated from the bubble collapse results directly from matching the pressure boundary conditions across the bubble wall as the gas is adiabatically compressed during the collapse (i.e. the Gilmore model does not include the blast wave). Nevertheless its overriding advantage is its ability to predict the bubble dynamics over the hundreds of microseconds for which a single cavitation event will persist during such lithotripter shock–bubble interactions (Leighton & Cleveland 2010).

The current paper extends the free-Lagrange simulation technique studied previously (Jamaluddin, Ball & Leighton 2002, 2004; Turangan *et al.* 2008) to introduce a method for predicting the far-field pressures resulting from the first collapse. The laboratory and patient trials conducted with the device that monitors these far-field pressure emissions found that for the vast majority of cases in both laboratory and patient trials, the far-field emissions from this first event exceeded those of later collapse cycles (see, e.g. figure 9 of Leighton *et al.* 2008*c*). Such patient data are invaluable in providing an endpoint to which bridges must be built from the simulations conducted here. Such bridges are found in the careful laboratory experimentation which elucidates the factors which influence the interactions between the stone, bubble and the incident and cavitation shock waves and their reflections (Calvisi *et al.* 2007, 2008; Iloreta *et al.* 2008).

Two projects were proposed to extend the time scales over which the numerical scheme used here (free-Lagrange method, FLM) could be applied. The first was to use FLM to simulate both the initial shock–bubble interaction and the later collapse (both types of behaviour having individually been simulated by Turangan *et al.* 2008), but coupling the two through use of the Gilmore model to cover the prolonged expansion phase. Funding could not be obtained for this study, and its role in developing the clinical device was filled in by laboratory tests (Fedele 2008). The second was to compare the FLM predictions with the dynamics of laser-induced bubbles, as a proxy for isolating the collapse which occurs after the prolonged expansion phase. However, such studies proved to be of limited use in this project because, although post-event damage on solid specimens in the proximity of the cavitation collapse was readily quantified, real-time monitoring of the erosion caused by such events showed significant amounts of that damage occurred before the cavitation collapse as a result of the initial interaction of the laser with the liquid (Hirsimaki *et al.* 2006).

Cavitation erosion is well known for the deleterious effects it produces to structures. Indeed this has been correlated with acoustic emission and vibration (van der Meulen 1986*a*,*b*; O'Leary *et al.* 1997; Leighton *et al.* 2003). However, cavitation erosion has been beneficial for some applications, such as in (cavitation) cleaning (Zequiri, Hodnett & Leighton 1997; Leighton *et al.* 2005; Birkin, Offin & Leighton 2005*b*), muscle injury therapy (Jarvinen *et al.* 2005), SWL (Coleman *et al.* 1987; Takayama 1999; Delius 2000), dental ultrasonics (O'Leary *et al.* 1997; Lea, Price & Walmsley 2005) and lipoplasty (e.g. in ultrasound-assisted lipoplasty (UAL) to remove excessive fat deposit under the skin; Cooter *et al.* 2001). Besides cavitation erosion, adiabatic compression of cavitation bubbles that leads to hot spot creation was also identified as one of the mechanisms by which explosion can start in commercial explosives (Coley & Field 1973; Chaudhri & Field 1974; Field, Swallowe & Heavens 1982; Bourne & Field 1991; Field 1994) and sometimes in accidental explosions during the transport of energetic materials (Kendrinskii 1997). If the cavitation occurs close to a boundary, or if the bubble collapse is itself caused by an incident shock wave (Field 1994), then the bubble can form a high-speed jet that passes through the bubble (as first suggested by Kornfeld & Suvorov 1944), a process which, upon impact of the jet against the downstream bubble surface, emits an intense blast wave (Lauterborn & Kurz 2010). A recent review by Lauterborn & Kurz (2010) has given much detail about the physics of bubble oscillations.

Depending on the initial bubble size (Leighton 2007), shock–bubble interaction is an extremely violent event. The high-speed jet may exceed $1\,\mathrm{km\,s^{-1}}$ and its impact can generate an intense blast wave exceeding 1 GPa in strength (Jamaluddin *et al.* 2004; Jamaluddin 2005). For even stronger incident shock waves, the jet velocity could reach up to $8000 \pm 4000\,\mathrm{m\,s^{-1}}$ as observed experimentally by Bourne & Field (1991) in experiments of shock-induced collapse of a 2D cavity. In related studies, luminescence was also observed (Dear, Field & Walton 1988; Bourne & Field 1991; Field 1994; Leighton 1994; Bourne & Field 1999; Bourne & Milne 2003). The phenomena of high-speed jet impingement and blast wave emission from jet impact are relevant to SWL as probably the main mechanisms of adverse effects. Moreover (and in particular with respect to the formation of surface cracks), they are significant contributors to stone fragmentation, together with the impact of the shock wave on the stone and the subsequent evolution of stress inside the stone (Zhu *et al.* 2002; Leighton & Cleveland 2010). Studies in shock–bubble interaction include experiments using high-speed photography of several thousand to a few million frames per second (Tomita & Shima 1986; Dear & Field 1988; Bourne & Field 1991; Ohl *et al.* 1999; Sankin *et al.* 2005). The use of lasers to generate a single cavitation bubble in liquid pioneered by Lauterborn (1972) and later popularised by him and his co-workers (Vogel, Lauterborn & Timm 1989; Philipp & Lauterborn 1998; Ohl *et al.* 1999; Brujan *et al.* 2001; Lindau & Lauterborn 2003) is now considered a standard practice because of its advantages in controlling key parameters of the bubble (although in this programme of work, real-time monitoring of erosion was necessary to determine how much damage was caused by the main cavitation event, and how much by the initial interaction of the laser with the liquid; Hirsimaki *et al.* 2006).

Other studies are via modelling/simulations such as the use of the Gilmore model (Church 1989), arbitrary Lagrangian–Eulerian method (Ding & Gracewski 1996), boundary element method (BEM) (Klaseboer *et al.* 2006, 2007), interface capturing weighted essentially non-oscillatory (WENO) schemes (Johnsen & Colonius 2009) and the FLM (Ball *et al.* 2000; Jamaluddin 2005; Turangan *et al.* 2008). BEM has been an extremely popular method in bubble dynamics simulations (Blake *et al.* 1986,

1997; Tong *et al.* 1999; Fong *et al.* 2006; Klaseboer *et al.* 2006; Turangan *et al.* 2006). Although the model assumes that the liquid phase is incompressible and the scalar properties of the gas are spatially uniform, Klaseboer *et al.* (2006, 2007) have shown that with some assumptions, BEM is still applicable to limited applications of shock–bubble interaction. FLM, on the other hand, has advantages over other simulation methods mentioned above that include its suitability for highly deforming flow, ability to sharply resolve material interfaces and to capture flow discontinuities, e.g. shock waves, as it takes into account the liquid compressibility. Apart from the Gilmore model, all the techniques mentioned in this paragraph are sufficiently computationally intensive that the computational domain (in both space and time) is restricted to less than the duration of the shock–bubble interactions that occur during lithotripsy. Certainly, the resources available to most projects could not simulate the pressure fields of interest to this project, which are at ranges of $O(10\,\mathrm{cm})$.

Many applications require a far-field acoustic emission prediction from fluid dynamics disturbances, e.g. helicopter rotor noise. Various schemes have been proposed such as the direct method that solves the Navier–Stokes equations and simultaneously solves the flow field and acoustic propagation. However, this method is computationally expensive and requires a huge domain. Our current study explores a more efficient technique to predict the far-field acoustic emissions whereby these emissions could be obtained using near-field solutions. This is done by separating the computational domain into a primary region that covers the nonlinear area where the flow is solved using suitable fluid dynamics methods, and a secondary region that covers the linear area where acoustic schemes are used (e.g. the Kirchhoff and Ffowcs Williams-Hawkings (FW-H) methods). The Kirchhoff and FW-H methods are attractive as they use surface integrals instead of volume integrals over the primary region for the far-field acoustic emission prediction, and have been applied to various aeroacoustic problems, e.g. helicopter, jet and propeller noise.

The Kirchhoff method assumes that the acoustic transmission is governed by a simple wave equation (Farassat & Myers 1988). It provides a link between the nonlinear near field of the flow and the acoustically linear far field. A control surface is assumed to enclose all the nonlinear effects and sound sources in the near field (Lyrintzis & George 1989; Lyrintzis & Xue 1991). Its main advantages are its simplicity and accuracy. The surface integrals and the required input parameters (the derivatives of pressure) on the control surface can be evaluated from suitable fluid dynamics data. One disadvantage is that the control surface must be placed in the linear region such that the input parameters are compatible with linear wave propagation. As the linear region is not well defined, the control surface must be positioned well away from the acoustic sources, but in most cases the solutions are not well resolved away from the source and require a fine mesh to ensure accurate wave resolution.

The FW-H equation for the aerodynamic sound radiated by a moving object is an exact rearrangement of the continuity and the Navier–Stokes equations in the form of an inhomogeneous wave equation with surface sources (monopole and dipole) and volume source (quadrupole) (di Francescantonio 1997). The monopole and dipole terms are easy to evaluate as they are surface integrals over the control surface. The major difficulty is that the quadrupole terms evaluation requires a volume integral calculation. This method has several advantages over the Kirchhoff method. First, each of the three sources in the FW-H formulation has physical meaning that helps understanding of the generation of the pressure field. The monopole component is determined by the geometry and kinematics of the body. The dipole component is

generated by the force acting on the fluid due to the presence of the body. The quadrupole component accounts for nonlinear wave effects, e.g. variations in the local sound speed, turbulence and contributions from shocks. Second, FW-H does not require the flow to obey the linear wave equation at the control surface, so it is less vulnerable to error if there is some moderate level of nonlinearity in the acoustic field at the control surface.

Our objectives were to simulate the fluid dynamics events associated with the shock–bubble interaction in shock wave lithotripsy for various scenarios (in a free field and near a rigid wall) using the free-Lagrange numerical scheme, and to show how, with sufficient computing power, it is possible to replace the Gilmore equation predictions of the far-field acoustic emissions caused by the associated cavitation events with predictions made by coupling of fluid dynamics data using the correct (blast wave) source for the dominant component. The impetus for generating this capability was to identify trends and mechanisms sufficient to support the development of an acoustic sensor that ultimately was used as an indicator of stone fragmentation and targeting in SWL (Leighton *et al.* 2008*c*) to give early warning of stones that will not respond to SWL (Fedele *et al.* 2010; Leighton & Cleveland 2010). Leighton *et al.* (2008*a*) provide the overview of how these simulations fitted into the research programme of simulation and experimentation to develop the sensor. This article covers the following material: the numerical schemes for the free-Lagrange numerical method and acoustic emissions are presented in § 2. The simulation of the lithotripter shock–bubble interactions in a free field are detailed in § 3 and the interactions near a rigid wall in § 4, together with a description of the method for predicting the far-field acoustic emissions of the cavitation events.

2. Free-Lagrange method and acoustic emission schemes

2.1. *Free-Lagrange method*

The FLM code, Vucalm, used in the simulations presented here was initially developed for 2D simulations (Ball 1996; Ball *et al.* 2000). Substantial further development of the code was carried out for simulations involving solid material with strength in order to model for high and hypervelocity impact problems (Howell & Ball 2002) and simulations in axisymmetric geometry (Jamaluddin *et al.* 2002, 2004; Leighton 2004; Turangan 2004; Jamaluddin 2005; Turangan *et al.* 2008). Vucalm solves the unsteady, compressible Euler equations on an unstructured Lagrangian finite-volume mesh. The method allows the mesh to convect with the local flow velocity, which results in the absence of advective fluxes. Consequently, features such as material interfaces are sharply resolved at all times. Allowing the mesh to change its connectivity freely prevents the severe mesh distortion associated with conventional Lagrangian schemes in which fixed mesh connectivity is adopted.

Vucalm uses a Voronoi mesh, the construction of which is based on computational particles that initially fill the computational domain (figure 1*a*). The mesh forms polygonal cells that enclose each particle and the region closest to the particle (Ball 1996). These particles are assigned with fluid type, thermodynamic properties, coordinates and flow conditions. Vucalm employs Riemann solvers (Godunov-type) with nominal second-order accuracy in space and first-order in time to compute the numerical fluxes across cell boundaries to update the flow density, velocities and temperature. If the cell represents a material with strength, e.g. aluminium, edge-oriented normal and shear stresses are computed to update the deviatoric stresses (Howell & Ball 2002; Turangan *et al.* 2008).

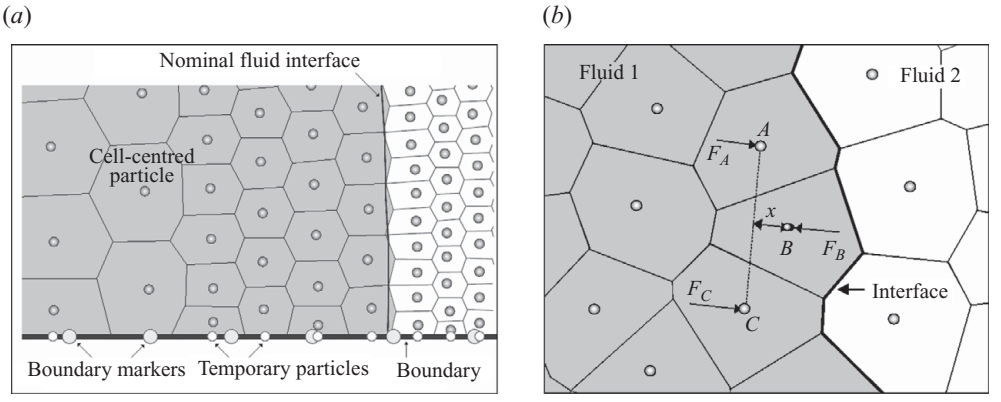

FIGURE 1. (*a*) Voronoi mesh used in FLM simulations. Nominal fluid interfaces are normally drawn for plotting purposes as the actual interface is determined by the cell boundaries shared by the dissimilar fluids. (*b*) Artificial surface tension: an irregularity on the interface between Fluid 1 and Fluid 2 is shown where a target particle B is off the line joining neighbours A and C by a distance x. Restoring forces F_A, F_B and F_C are applied to A, B and C, respectively so as to drive x towards zero to maintain a 'smooth interface.'

As each Voronoi cell represents an individual fluid type, material interfaces always coincide with the Voronoi cell boundaries. However, the interfaces tend to wrinkle on a scale comparable to the mesh resolution, which may grow when subjected to mesh-induced high-wavenumber instabilities. To minimize these instabilities, an interface smoothing algorithm has been incorporated into Vucalm by adding a source term that constitutes a force to the governing equations (Howell & Ball 2000). This acts as an artificial surface tension applied only to particles adjacent to the interfaces, which reduces both the amplitude and growth rate of small-scale perturbations (figure 1*b*).

A validation of Vucalm for a shock-induced bubble collapse problem has been presented previously in Jamaluddin (2005) and Turangan *et al.* (2008). It involves a scenario where a spherical bubble of 1.0 mm in radius is collapsed by a 0.528 GPa planar shock. The result was compared with the arbitrary Lagrangian–Eulerian (ALE) simulation (Ding & Gracewski 1996). Not only did the FLM simulation match the predictions of the ALE code in capturing the phenomena of bubble jetting and jet velocity profile, it also demonstrates a better shock resolution particularly within and in the vicinity of the bubble, and is able to continue beyond the jet impact event showing the emission of the intense blast wave and the toroidal bubble formation, which the ALE simulation was not able to attain.

2.2. *Acoustic emission schemes*

To estimate the acoustic emission in the far field generated by a shock–bubble interaction, two acoustic emission numerical codes were developed using the Kirchhoff and FW-H formulations. The integral formulations of these schemes allow radiating sounds to be evaluated based on quantities recorded on an arbitrary near-field control surface that encloses the sound sources. The codes predict the far-field acoustic emissions that would be recorded by an observer located anywhere outside the source region. This is accomplished using two steps (figure 2). First, Vucalm is used to evaluate the flow field in the near field and on the control surface. Second, the information from the control surface is then used to determine the far-field emissions by means of the acoustic emission codes. Current computational limitations preclude the option of using Vucalm on its own to simulate the entire flow field and record the

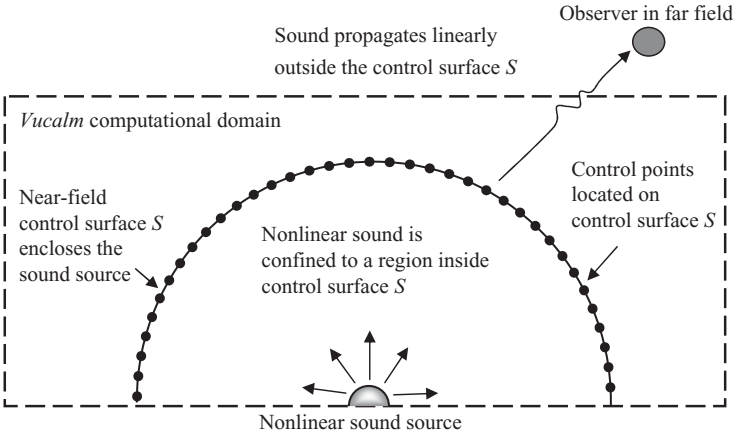

FIGURE 2. Schematic of Vucalm and acoustic emission simulation coupling. The Vucalm domain encloses the sound source, the control surface S and control points. The nonlinear sound propagation is confined inside S, and the sounds are assumed to propagate linearly outside S. An observer is placed in the far field where the acoustic emissions are to be recorded.

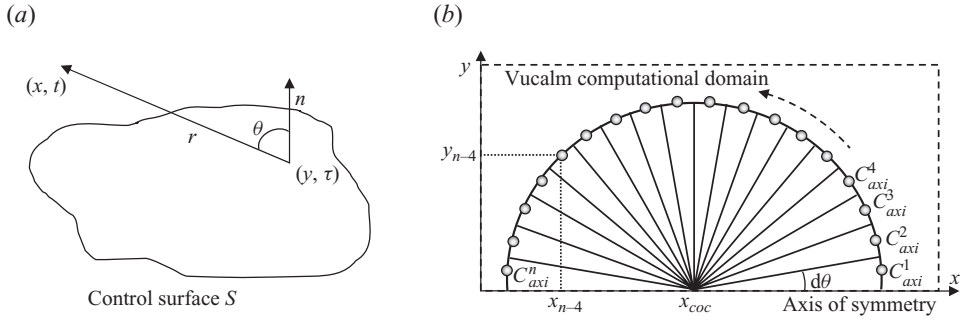

FIGURE 3. (a) Kirchhoff's control surface S. θ is the angle between the normal vector on the surface $\boldsymbol{n}$ and the radiation vector $\boldsymbol{r}$. (b) For the axisymmetric case, Kirchhoff's control points $(C^i_{axi}, \ldots, C^n_{axi})$ are placed on the circumference of the semicircle that is rotated about the axis of symmetry.

far-field acoustic emissions as this would require an excessively huge computational domain. Indeed, current computational facilities will not always be sufficient for the less demanding but more practicable task of calculating the flow field out to a sufficient range of the control surface, such that propagation beyond that control surface is always linear. One of the objectives of this paper is to demonstrate the techniques to allow such calculations when such computational power becomes readily accessible.

2.2.1. *The Kirchhoff formulation*

For a stationary control surface S (figure 3a), the Kirchhoff formulation (Farassat & Myers 1988) that gives the far-field emission of sources (e.g. acoustic) confined within S can be written as

$$\Phi(\boldsymbol{x}, t) = \frac{1}{4\pi} \int_S \left[\frac{\Phi}{r^2} \frac{\partial \boldsymbol{r}}{\partial \boldsymbol{n}} - \frac{1}{r} \frac{\partial \Phi}{\partial \boldsymbol{n}} + \frac{1}{c\, r} \frac{\partial \boldsymbol{r}}{\partial \boldsymbol{n}} \frac{\partial \Phi}{\partial \tau} \right]_\tau \mathrm{d}S, \tag{2.1}$$

where Φ is a quantity satisfying the wave equation outside S, c is the sound speed at ambient conditions and $\boldsymbol{n}$ is the normal vector on the surface. Here, Φ is a

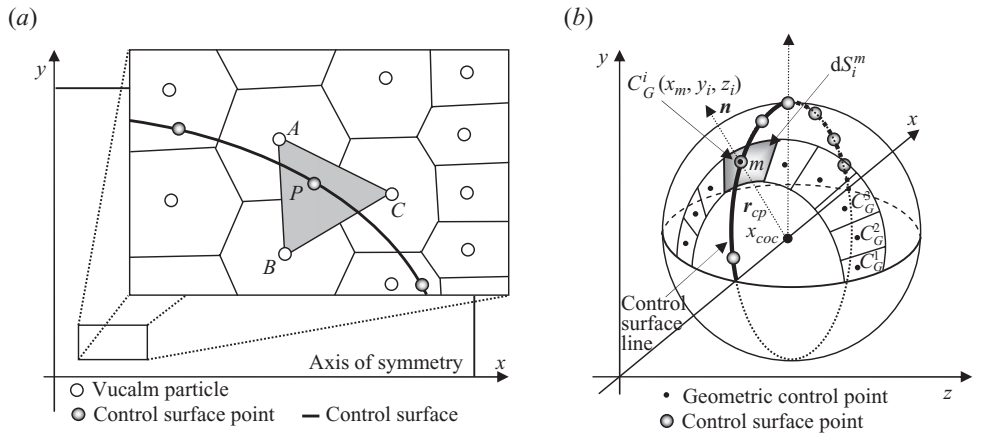

FIGURE 4. (*a*) Interpolation from Vucalm particles to the Kirchhoff's control surface point. Three Vucalm particles of the same material (*A*, *B* and *C*) determine the values of p, $\partial p/\partial n$, $\partial p/\partial t$ of the Kirchhoff's control surface point *P*. (*b*) The values of p, $\partial p/\partial n$, $\partial p/\partial t$ of the control surface points are interpolated onto the geometric control points $(C^1_G, \ldots, C^j_G)$. For example, for the mth control surface point that has an elemental area $\mathrm{d}S^m_i$, the geometric control point $C^i_G(x_m, y_i, z_i) = C^m_{axi}(x_m, y_m)$. Superscript j indicates the number of geometric control points in one rotation.

pressure disturbance, p, and its normal and time derivatives ($\partial p/\partial n$ and $\partial p/\partial t$) must be continuous outside S. The surface S is assumed to be non-deformable and fixed in space, and encloses the sound sources and nonlinear effects. The subscript τ indicates the integrands are evaluated at the emission (retarded) time given by $\tau = t - \tau'$, where $\tau' = \boldsymbol{r}/c$ is the wave propagation time to observer, $\boldsymbol{r} = \boldsymbol{x} - \boldsymbol{y}$ is the radiation vector and $r = |\boldsymbol{x} - \boldsymbol{y}|$ is the distance between the observer and the source.

The Kirchhoff scheme requires stored time histories of p, $\partial p/\partial n$ and $\partial p/\partial t$ on the control surface, S. Since the scheme assumes that the linear wave equation is valid outside S, it must be large enough to contain the region of all nonlinear behaviour. In the present work, a sphere has been chosen for the control surface S, which is incorporated in the Vucalm computational domain via a semicircle that is rotated about the axis of symmetry. Control points are distributed uniformly along the circumference of the semicircle separated by a constant angle $\mathrm{d}\theta$ (figure 3*b*).

In Vucalm simulations, p, $\partial p/\partial n$, and $\partial p/\partial t$ are evaluated at the control surface points $(C^1_{axi}, \ldots, C^n_{axi})$ by a linear interpolation of those input parameters from three neighbouring Vucalm particles where the flow gradient is taken into account (figure 4*a*). For the far-field acoustic emission calculation, these data are stored and then interpolated onto the geometric control points $(C^1_G, \ldots, C^j_G)$ (figure 4*b*). The Kirchhoff integral is then evaluated through a summation of the contributions from each geometric control point to obtain the pressure at an arbitrary point outside S.

2.2.2. *The Ffowcs William–Hawkings formulation*

The FW-H formulation is derived directly from the conservation of mass and momentum. Therefore, it can be applied to an arbitrary surface whether or not the disturbance propagation is linear outside the control surface S. The nonlinear wave propagation is taken into account by the quadrupole source. The solution to the FW-H equation can be written as $p'(\boldsymbol{x}, t) = p'_T(\boldsymbol{x}, t) + p'_L(\boldsymbol{x}, t) + p'_Q(\boldsymbol{x}, t)$, where $p'(\boldsymbol{x}, t)$ is the far-field acoustic pressure outside the source region, and the subscripts T, L and Q represent the thickness (monopole), loading (dipole) and quadrupole sources

(di Francescantonio 1997). If the control surface S is sufficiently far from the source, the nonlinearity is taken into account by the surface integrals as the quadrupole source becomes negligible. Indeed, Brentner & Farassat (1998) argued that the solution is less sensitive to placement of the control surface even if the quadrupole source is neglected. Following Farassat & Succi (1983), where a stationary fictitious control surface S is used and the quadrupole source is negligible, the FW-H formulation (without the quadrupole source) is given by

$$p'(\boldsymbol{x}, t) = \frac{1}{4\pi}\left(\int \frac{\rho_0 \dot{U}_n}{r}\,\mathrm{d}S + \frac{1}{c}\int \frac{\dot{L}_r}{r}\,\mathrm{d}S + \int \frac{L_r}{r^2}\,\mathrm{d}S\right), \tag{2.2}$$

where U_n and L_r are the dot products of variables U_i and L_i with the unit vector in the normal direction $\hat{\boldsymbol{n}}$ and radiation direction $\hat{\boldsymbol{r}}$, respectively, c is the sound speed of the medium and r is the distance between the control point and the observer. The terms $\dot{U}_n$ and $\dot{L}_r$ are the rate of change of U_n and L_r, respectively, and $U_i = \rho\, u_i/\rho_0$ and $L_i = P_{ij}\,\hat{\boldsymbol{n}}_j + \rho u_i u_n$ where ρ_0 is the density of the medium (water) in the far field, ρ is the density of the fluid on S, u_i is the velocity at the control point, P_{ij} is the pressure at the control point on S, $\hat{\boldsymbol{n}}_j$ is the unit vector normal to S and u_n is the fluid velocity at the control point in the direction normal to S. This FW-H scheme is applicable to the Kirchhoff-type surface and therefore their discretization techniques and control surface geometries are similar.

The interpretation of (2.1) and (2.2) is that the integration occurs over a surface. The integration is calculated at the emission or retarded time that is the same as that recorded in the Vucalm simulation. The formulation requires that the observer time t and location $\boldsymbol{x}$ are fixed during the integral evaluation. Because the retarded time formulation is used, temporal interpolation of the input data is required. Time histories of p', ρ and ρu_i are stored by choosing both the observer position and the observer time, evaluating the surface integrals and then stepping to the next observer time in the time history.

Hence, in the Vucalm simulation, the input data are expediently evaluated at the control points by spatial interpolation at the source time. At the end of the simulation, a time history of the required data is stored and utilized in the acoustic emission codes. A time increment of the observer time is specified by the user and the upper and lower integral limits are calculated based on the duration of the recorded Vucalm data. Following this, a temporal interpolation of the data to the retarded time τ at each location in the input data is performed. The retarded time for each control point is simply the difference between the observer time t and the wave radiation time from the corresponding control point to the observer. Interpolation in time is necessary so that the contributions from all control points can be added together at the same observer time.

The FW-H requires the storage of ρ, p' and ρu_i for each control point, and the Kirchhoff requires p, $\partial p/\partial n$ and $\partial p/\partial t$. The Kirchhoff method is simpler and easier to implement but assumes a solution of the linear wave equation on surface S. The FW-H method, however, allows for nonlinearities on S. Therefore, if the Vucalm solution does not satisfy the linear wave equation on the control surface, the results from the Kirchhoff method change dramatically, which leads to a higher sensitivity for the control surface location.

2.2.3. *Validation of the acoustic emission codes*

The validation of the Kirchhoff scheme involves predicting the far-field acoustic emissions radiated by a rigid pulsator in water and comparing those to the analytical

solution. The rigid pulsator is a sphere that changes volume without a commensurate change in the pressure within the sphere, so that wall motion alone is responsible for the radiation of a spherical sinusoidal wave into the surrounding water (Leighton 1994).

For the Kirchhoff validation case, the variation of pulsator radius with time is defined by $R(t) = R_0 - R_{\varepsilon 0}\,\mathrm{e}^{\mathrm{i}wt}$, where R_0 is the equilibrium radius and $R_{\varepsilon 0}$ is the pulsator radial displacement amplitude. The acoustic pressure at any radius $r \geqslant R_0$ is given by

$$P(r,t) = \rho_0 c U_0 \frac{R_0}{r} \cos X_0\, \mathrm{e}^{(\mathrm{i}\omega t - k(r-R_0)+X_0)} \tag{2.3}$$

whose magnitude is $|P(r,t)| = (\rho_0 c |U_0| R_0^2 k)/(r\sqrt{1+(kR_0)^2})$, where ρ_0 is the equilibrium fluid density, c is the speed of acoustic waves, $U_0 = -i\omega R_{\varepsilon 0}$ must be equal to the radial fluid particle velocity $\dot{\varepsilon}$ at the pulsator wall at all times, $\cos X_0 = kR_0/\sqrt{1+k^2R_0^2}$, $R_0 = 0.02$ mm and k is the wavenumber. The near-field pressure–time history at every control point on the control surface S is calculated from $|P(r,t)|$. The normal and time derivatives of pressure are obtained from (2.3) and substituted into (2.1). The analytical solution is directly calculated from (2.3) for a single far-field observer.

For the analysis, an observer is positioned at 500 mm from the centre of the oscillating pulsator, i.e. $\boldsymbol{x} = (0, 500\,\mathrm{mm}, 0)$. The parameters of the driving pressure are: $\omega = 4.7837 \times 10^6\ \mathrm{s}^{-1}$ ($f = 7.6 \times 10^5$ Hz), $U_0 = 20\ \mathrm{m\,s}^{-1}$, the period is 1.313 µs and the wavelength in water is 2 mm. The results of tests carried out for a range of control surface radii R_{cs} ($1\,\mathrm{mm} \leqslant R_{cs} \leqslant 2\,\mathrm{mm}$) are presented in figure 5(*a*). Jamaluddin (2005) also conducted tests for larger R_{cs} ($10\,\mathrm{mm} \leqslant R_{cs} \leqslant 20\,\mathrm{mm}$). Both the prediction and analytical solution for two different ranges of R_{cs} give the same far-field acoustic emissions and therefore they are independent of the size of R_{cs} for the small-amplitude waves used in this validation.

For the FW-H scheme test, a different set of equations for pressure and velocity are used to take into account the phase difference between the two terms from near field to the far field because accurate knowledge is required of both the particle velocity on the surface and the volume integral of the FW-H scheme. The amplitude of the test signals for the FW-H test problems satisfies the linear wave equation. The validation test case involves an analysis of a spherical spreading wave originating from a point source. First, consider that the acoustic particle velocity in the r direction, U, is in phase with the acoustic pressure, p, everywhere in the far field of a simple acoustic source radiating spherical waves. In the far field, p and U are related by the characteristic impedance as $p(r,t)/U(r,t) = \rho c$. In the near field of a time harmonic source, the pressure is given by

$$p = -\mathrm{i}Q_S \frac{\mathrm{e}^{\mathrm{i}k(r-ct)}}{r}. \tag{2.4}$$

The corresponding particle velocity component in the r direction is

$$U = \frac{1}{\rho c}\left(1 + \frac{i}{kr}\right) p \tag{2.5}$$

whose real parts of pressure and velocity are given as

$$p(r,t) = \frac{Q_\mathrm{s}}{r} \sin\omega\left(\frac{r}{c} - t\right) \quad \text{and} \quad U(r,t) = \frac{Q_\mathrm{s}}{\rho r c} \sin\omega\left(\frac{r}{c} - t\right) + \frac{Q_\mathrm{s}}{k\rho r^2 c} \cos\omega\left(\frac{r}{c} - t\right), \tag{2.6}$$

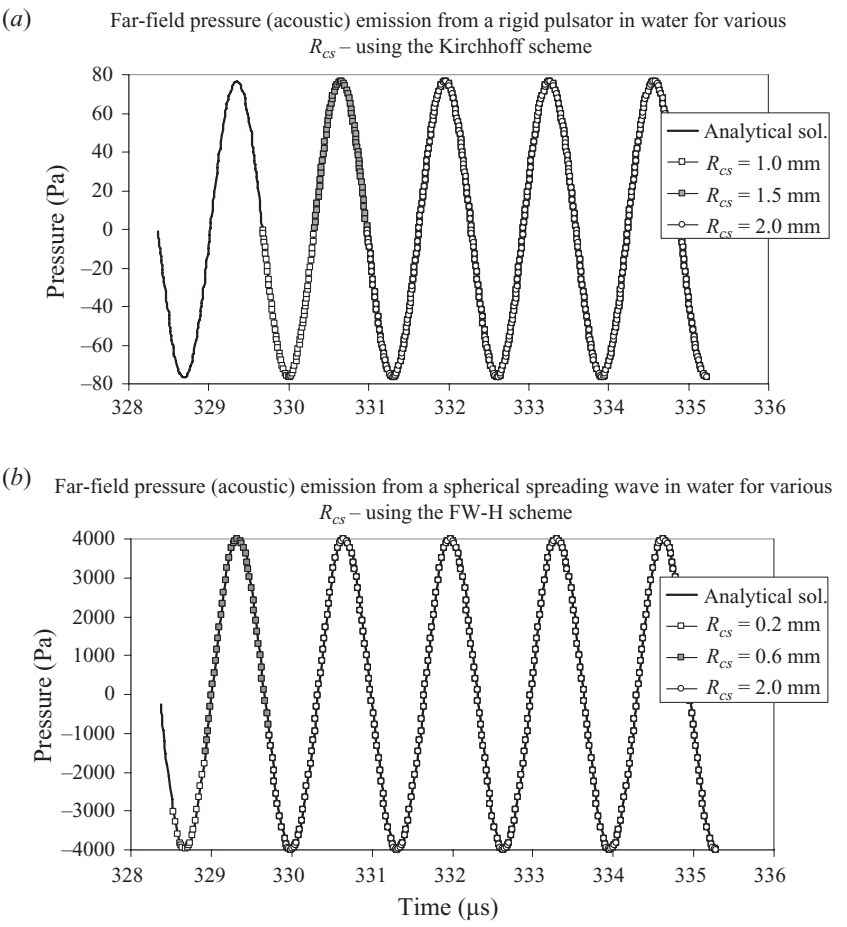

FIGURE 5. Comparisons of the far-field acoustic emissions by an observer located at $\boldsymbol{x} = (0, 500\,\text{mm}, 0)$ with the analytical solution using the Kirchhoff and FW-H schemes for: (*a*) small amplitude driving pressure, (*b*) large amplitude driving pressure. Refer to the text for driving pressure parameters.

respectively. These equations of pressure and velocity are used to generate the data at the control points for input to the FW-H integral for the far-field calculation. Tests were carried out to examine the dependencies on the control surface radius R_{cs} for the stated range ($0.2\,\text{mm} \leqslant R_{cs} \leqslant 2.0\,\text{mm}$) (figure 5*b*). The parameters of the driving pressure are: $\omega = 4.7837 \times 10^6\,\text{s}^{-1}$ ($f = 7.6 \times 10^5\,\text{Hz}$), pressure amplitude $Q_S = 2.0 \times 10^3\,\text{Pa}$, the period is 1.313 μs and the wavelength in water is 2 mm. The results for larger R_{cs} ($5.0\,\text{mm} \leqslant R_{cs} \leqslant 7.5\,\text{mm}$) are also presented by Jamaluddin (2005). The predicted far-field emissions are independent of control surface placement and in agreement with the analytical solution. It should be stressed that these validation exercises are undertaken against a rigid sphere analytical prediction, which includes only linear dynamics, so does not fully explore the ability of the codes to encompass nonlinear features. This aspect will be explored more fully in § 3.4.

Thermodynamic properties	Water	Air (bubble)
Density, ρ (kg m^{-3})	1000	1.2246
Pressure, P (kPa)	101.325	101.325
Temperature, T (K)	288.15	288.15
Specific heat ratio, γ	–	1.4

TABLE 1. Properties of water and air bubble at standard atmospheric conditions.

3. Lithotripter shock–bubble interaction in a free field

3.1. *Mesh resolution and artificial surface tension*

A mesh resolution study was initially performed to determine the optimum mesh resolution required to capture the shock–bubble interaction events at minimal computational cost. It involves a scenario where a lithotripter shock in water collapses an initially spherical bubble immersed in water. The initial radius R_0 was set at 0.04 mm, because *in vivo* experiments suggested initial radii of 0.04–0.06 mm are of typical size (Coleman & Saunders 1989; Cunningham *et al.* 2001; Turangan *et al.* 2008). The bubble is located near a rigid wall at a distance $d = 0.0425$ mm. The wall is represented by a fully-reflecting boundary of the computational domain. The lithotripter shock, modelled to propagate towards the bubble and the wall, consists of a $P^+ = 60$ MPa compressive wave and a $P^- = 10$ MPa tensile wave. Its analytical expression can be written as

$$P_s(t) = 2\,P_s\,\mathrm{e}^{-\beta_d t}\,\cos(\omega t + \pi/3), \tag{3.1}$$

where P_s is the shock amplitude that equals the positive peak pressure P^+ when the rise time is zero, $\beta_d = 9.1 \times 10^5\ \mathrm{s}^{-1}$ is the decay constant and $\omega = 2\pi f$ where $f = 83.3$ kHz (Church 1989). The water is represented by the Tait equation of state (EOS) and the air bubble by the ideal gas EOS. The flow initial conditions are given in table 1.

Three cases were tested: coarse mesh (6135 cells), intermediate mesh (32 085 cells) and fine mesh (77 406 cells). In the simulations, these cell numbers changed slightly as a result of an adaptive mesh refinement procedure employed to prevent a mismatch in cell area ratio particularly around the bubble interface. As indicated by bubble volume–time histories (figure 6*a*), the intermediate and fine mesh curves are in good agreement from the start until the time when the simulation was stopped. The collapse rate in the coarse mesh case is greater than that of the other two cases (apparent from $t = 0$ to $t \approx 0.21$ μs). The intermediate mesh is optimum in capturing the dynamics of the collapse and therefore, it was used for the subsequent simulations.

For the artificial surface tension (see § 2.1), it was necessary to determine the required value of a non-dimensional smoothing gain, α, associated with its restoring force. The choice, however, is currently based on user experience. We performed a study by running three simulations with different α to determine the optimum α that allows the bubble to evolve naturally while effectively maintaining a smooth interface, and compared the results with that of $\alpha = 0$. The smoothing gains, α, tested are 4×10^3, 8×10^3 and 16×10^3, obtained via trial and error. In the early stage of collapse, bubble deformation is minimal. Towards the final stage, the bubble undergoes a rapid deformation including its high-speed jet formation. The selection of a suitable α is thus made based on the comparison of the bubble evolution towards the end of the collapse. As Jamaluddin (2005) shows, for $\alpha = 0$, the highly shearing

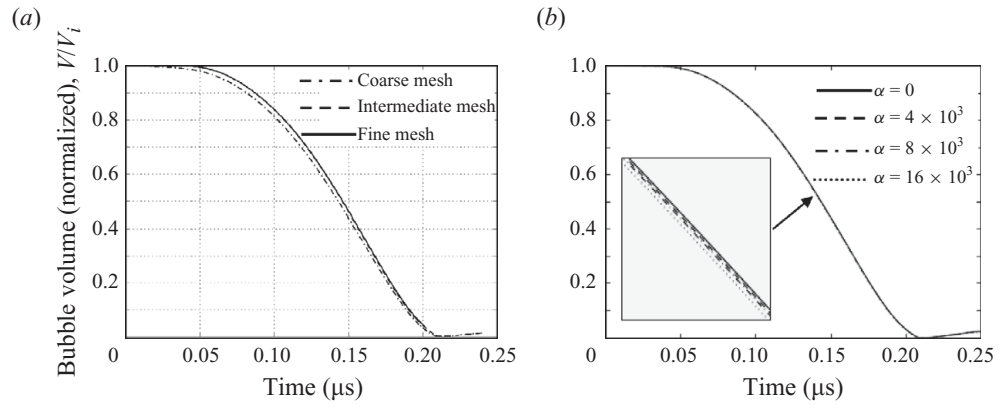

FIGURE 6. Plots of bubble volume–time history for: (*a*) mesh resolution (6135 cells for coarse, 32 085 for intermediate and 77 406 for fine mesh). Both the intermediate and fine mesh curves coincide. Note that the bubble collapse is non-symmetrical (it forms a jet) and its volume is calculated from the plots similar to figure 9 where V_i is the initial bubble volume. (*b*) Smoothing gains, α, for the artificial surface tension.

flow causes wrinkles on the bubble surface/interface. Increasing α to 4×10^3 improves the interface smoothness although signs of wrinkles still exist. For $\alpha = 8 \times 10^3$, the interface is smoother. When $\alpha = 16 \times 10^3$, the restoring force appears to be excessive and causes a slightly earlier collapse. Given that the simulation with $\alpha = 0$ is the gauge for correct physical features of bubble collapse, the comparison of bubble shape and its volume–time history (figure 6*b*) for various α shows that $\alpha = 8 \times 10^3$ is optimum, and hence it was used.

3.2. *Bubble dynamics*

For the lithotripter shock–bubble interaction in a free field, a spherical air bubble immersed in water is impacted by a lithotripter shock ($P^+ = 90$ MPa and $P^- = -10$ MPa) (figure 7). The shock is introduced by imposing a time-dependent pressure boundary condition on the left computational boundary. The initial conditions of the water and air bubble are standard atmospheric conditions (see table 1). The initial bubble radius R_0 is 0.06 mm. When comparisons were made between the 0.04 and 0.06 mm bubble radius cases, the dynamics of the collapsing bubble is similar. The only difference is in the duration of the collapse and a slight reduction in the magnitude of the blast wave when $R_0 = 0.06$ mm.

The sequence of this shock–bubble interaction is plotted in figure 9. As a result of the profound acoustic impedance mismatch, a relatively weak shock is transmitted into the air bubble when the lithotripter shock (indicated as IS in figure 8*a*) impacts the left bubble surface, whilst a strong expansion fan (EX) is reflected in the water. The shock in the bubble propagates more slowly and decouples from the incident shock. The high-speed flow behind the incident shock and the inertia of the water cause the bubble surface to form an impinging jet. The intersection of the shock and expansion waves at the bubble surface results in weakening and curvature of the shock (figure 9*a*).

The pressure gradient in the water near the bubble's upstream surface increases as time progresses. The collapse is non-spherical as the bubble's downstream surface remains nearly stationary up to just before $t = 0.19$ μs (figure 9*b*). At about $t = 0.20$ μs (figure 9*c*), the bubble's upstream surface starts to involute to form the high-speed

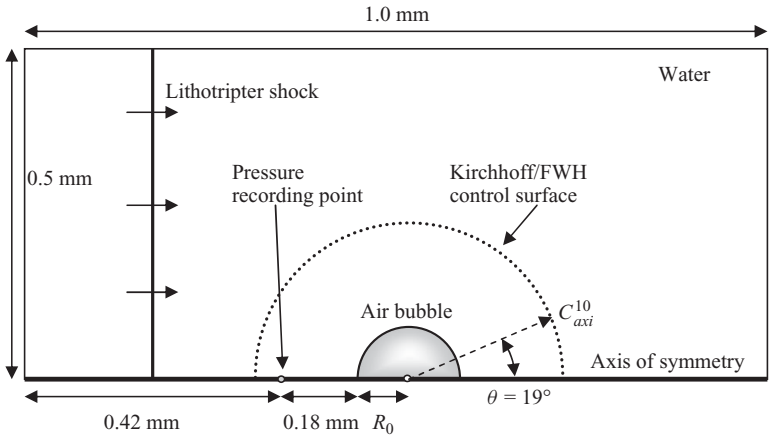

FIGURE 7. A bubble with initial radius $R_0 = 0.06$ mm located in a free field in water is impacted by a lithotripter shock ($P^+ = 90$ MPa, $P^- = -10$ MPa). The Kirchhoff/FW-H control surface radius $R_{cs} = 5\,R_0 = 0.2$ mm and 90 control points. Figure not to scale.

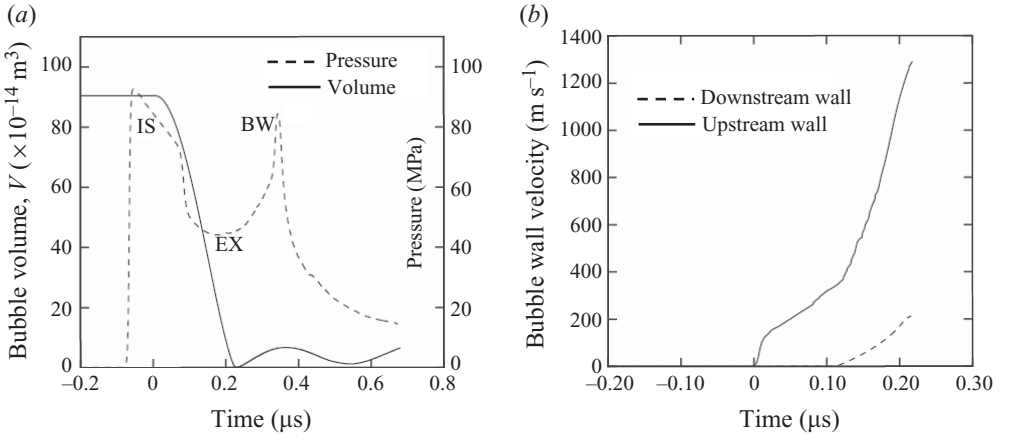

FIGURE 8. (*a*) Pressure- and bubble volume–time history. Pressure is measured at the recording point located on the axis of symmetry (see figure 7). Labelling: IS, lithotripter shock; EX, expansion waves; BW, blast wave; (*b*) Liquid jet velocity–time history.

liquid jet running to the right. The motion of the bubble during this phase is controlled almost exclusively by the water inertia. The liquid jet continues to accelerate and impacts the downstream surface at about $t = 0.221$ μs, forming a toroidal bubble of highly compressed air (figure 9*d*). The variation of jet velocity with time is shown in figure 8*b*). The jet continues to accelerate as it pierces the bubble with a maximum velocity of over 1.2 km s^{-1} attained immediately prior to the jet impact. It is believed that high-speed jets of this type play a primary role in cavitation erosion (Benjamin & Ellis 1966) as well as formation of circular pits and indentation on metal foils (Coleman *et al.* 1987). The development of real-time techniques for monitoring the formation of damage (Birkin, Offin & Leighton 2004*a*,*b*), and their correlation with high-speed photography (Vian, Birkin & Leighton 2010), should enable crucial tests in this area to be conducted. The initial collapse and all the bubble motion

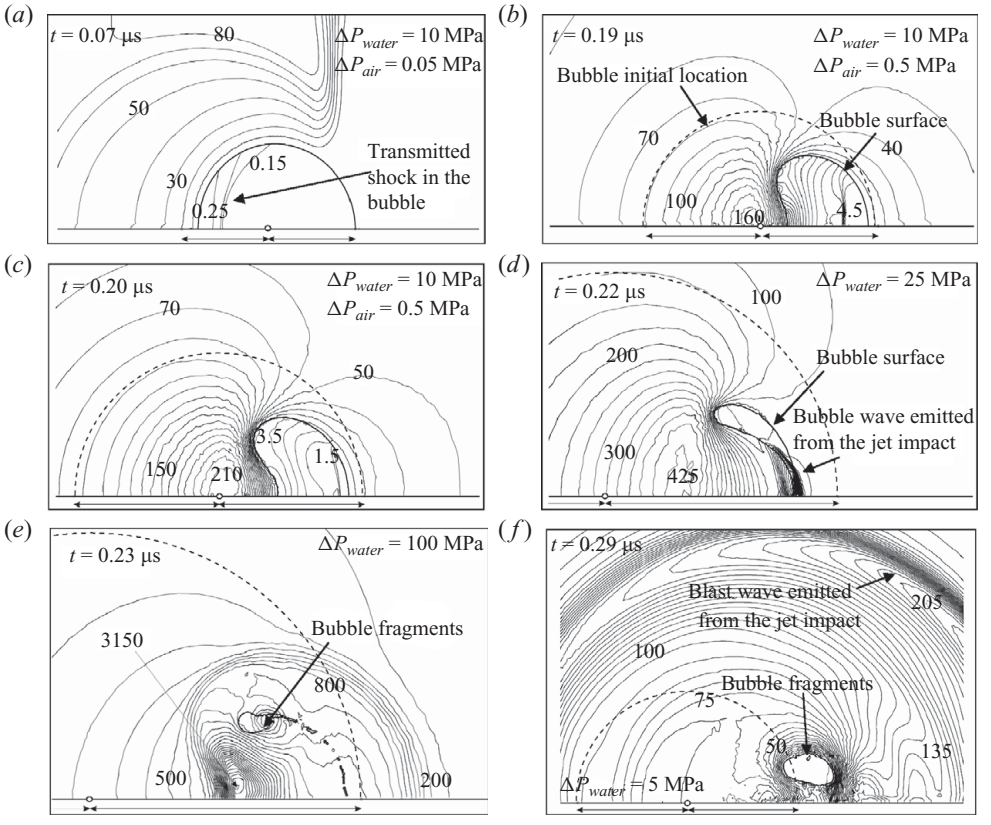

FIGURE 9. (*a*)–(*f*) Bubble evolution following its interaction with a lithotripter shock in a free field showing the high-speed jet formation, jet impact, blast wave emission and bubble fragmentation. The contours are of pressure with ΔP_{water} and ΔP_{air} indicating contour intervals in water and bubble, respectively. The initial location of bubble surface is indicated by the dashed line, and the two arrows below each panel indicate the initial bubble radii and meet below the initial bubble centre. An animation of a qualitatively similar collapse can be found on the Journal of Fluid Mechanics web page associated with Turangan *et al.* (2008).

shown in figure 9 are driven solely by the compressive wave of the lithotripter shock as the bubble does not encounter the tensile wave of the shock before the primary collapse is complete.

The impact of the jet on the bubble downstream surface emits an intense blast wave. It also leads to the creation of bubble fragments (figure 9*e*) that may coalesce with the main cavity or act as nuclei for further cavitation events. The most likely scenario is that these fragments expand and undergo some coalescence during the prolonged tensile tail of the lithotripter pulse (Leighton, Ho & Flaxman 1997; Leighton *et al.* 1998; Leighton, Cox & Phelps 2000). The peak overpressure exceeds 1 GPa. As a result of the high velocity of the liquid jet, the radiated blast wave advances relatively slowly to the left, and therefore its front in the vicinity of the jet impact is non-spherical. The interaction also produces a strong vortex flow. As depicted in figure 9(*e*), the air cavity is drawn into the vortex core while the blast wave continues to propagate outwards. The blast wave produces a sharp peak (BW) on the pressure–time history curve recorded at the pressure point (figure 8*a*) but its strength decreases exponentially

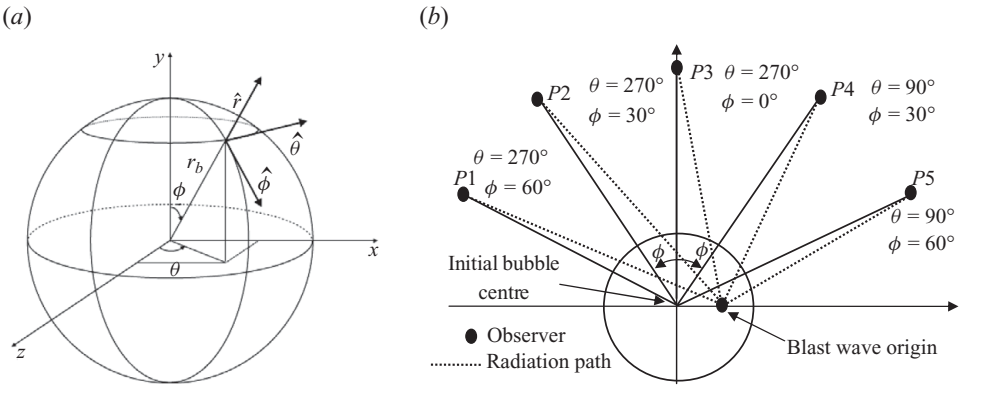

FIGURE 10. (*a*) Nomenclature and the acoustic emission problem geometry. (*b*) Blast wave radiation path to observer for five different θ and ϕ combinations on the XY-plane, which represents five observer's locations.

as it propagates radially into the surrounding water. The radiated blast wave could explain the large pressure spikes recorded by Zhong *et al.* (1997) near the primary collapse in their experiments.

The time history of the bubble volume (figure 8*a*) indicates a nearly linear reduction from when the bubble is impacted by the shock until its first minimum at $t \approx 0.22\,\mu s$. The end of the near-linear phase correlates with the liquid jet impact. At this time, the internal pressure greatly exceeds that of the surrounding water, and the bubble begins to expand, entering an oscillatory state with further cycles of expansions and collapses. The simulation was halted after the third collapse, but the Gilmore model predicts that when the bubble encounters the tensile portion of the lithotripter pulse it will enter a phase of prolonged expansion. This is followed by a series of damped oscillations that eventually tend to the natural frequency of the final bubble (Church 1989).

3.3. *Far-field acoustic emissions of bubble collapse in a free field calculated using the Kirchhoff and FW-H schemes*

The control surface, S, for the evaluation of the Kirchhoff and FW-H integrals (figure 7) has a radius $R_{cs} = 0.2\,mm$ and 90 control points placed along its half circumference. For the far-field acoustic emission calculation, the observer is placed at a distance $r_b = 150\,mm$ away from the initial bubble centre. This is chosen as it is a typical radiation wave distance from the lithotripter focal point to the sensor that is placed on the skin of the patient during clinical use of the sensor that these simulations were designed to support (Leighton *et al.* 2008*b*).

The nomenclature, geometry and reference frame for the acoustic emission problems are illustrated in figure 10(*a*). The nomenclature used for describing the observer position is identical to the one used for structuring and discretization of the spherical control surface in § 2.2. The reference frame (x, y, z) is analogous to the one used in the Vucalm formulation, i.e. the lithotripter shock propagates in the positive x direction. However, in Vucalm, the x-axis represents the axis of symmetry. The variables θ and ϕ are used to describe the position of the observer. Based on the geometry shown in figure 10(*a*), the polar coordinates for any point on the control surface

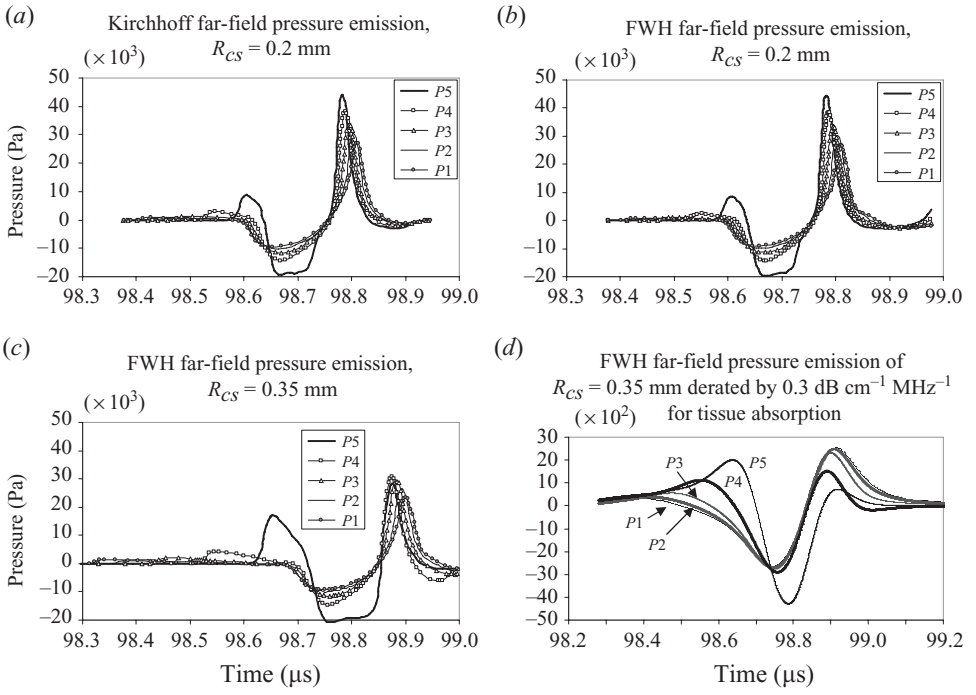

FIGURE 11. The far-field acoustic emissions read by an observer located at 150 mm from the initial bubble centre for five θ and ϕ combinations (i.e. observer's locations denoted by $P1$–$P5$ – refer to figure 10). (*a*) Kirchhoff scheme with $R_{cs} = 0.2$ mm, (*b*) FW-H scheme with $R_{cs} = 0.2$ mm, (*c*) FW-H scheme with $R_{cs} = 0.35$ mm, (*d*) the data of frame (*c*) derated by the standard value of 0.3 dB cm^{-1} MHz^{-1} to include the effect of absorption in tissue.

and the observer are given by ($x = r_b \sin\theta \sin\phi$, $y = r_b \cos\phi$, $z = r_b \cos\theta \sin\phi$) where $r_b^2 = x^2 + y^2 + z^2$.

Figure 11(*a*) shows the pressure–time history calculated in the far field using the Kirchhoff formulation. Results for various θ and ϕ are plotted for comparison to determine the variation in the far-field pressure profile at different observer positions and the dependency on the directionality of the lithotripter shock. The same set of Vucalm simulation data was used for all calculations.

Comparison of the near-field pressure–time history (figure 8*a*) with the predicted far-field acoustic waveforms using the Kirchhoff method (figure 11*a*) shows that both pressure profiles have similar characteristics. The trough of the expansion wave and the sharp peak of the spherical blast wave generated by the liquid jet impact are well captured. Owing to the non-symmetrical nature of bubble collapse, the peak positive pressure of the blast wave is greater when $\theta = 90°$. For this location, the observer is positioned closer to the origin of the blast wave, compared to when $\theta = 270°$. As the observer position is rotated on the XY-plane from $\theta = 90°$, $\phi = 60°$ (P5) to $\theta = 270°$, $\phi = 60°$ (P1), the waves travel longer distances to the observer. It might suggest that the signal strength changes with location because the pressure amplitude seen by the observer decreases. However, since $R_{cs} = 0.2$ mm and $r_b = 150$ mm, the maximum variation in path length for the blast wave with θ is only of the order of 0.05 %. Therefore, it is believed that the directional nature of the blast wave is more likely to explain the observations.

The advantages and disadvantages of the FW-H and the Kirchhoff formulations are discussed in § 2.2, but the deciding factor is how well these methods compare in practice. The main advantage in applying the FW-H equation on a Kirchhoff-type integration surface is that the coupling with fluid dynamics codes is easier because the normal derivative of pressure is no longer required (di Francescantonio 1997). Furthermore, the calculations carried out in this work do not include the quadrupole source terms, which greatly simplifies the acoustical problem. The numerical accuracies of both the Kirchhoff and FW-H codes are very similar because the quadrature is based on the Vucalm mesh, and therefore the time computations and quadrature points are identical for these two codes. Moreover, the characteristics of the control surface are identical, and similar discretizations of the surface and spatial interpolation techniques for the input data are implemented.

The results of the predicted far-field noise using the FW-H scheme for $R_{cs} = 0.2$ mm and $R_{cs} = 0.35$ mm are shown in figures 11(*b*) and 11(*c*) respectively. The results for $R_{cs} = 0.2$ mm agree with those of the Kirchhoff results (figure 11*a*). As R_{cs} is increased to 0.35 mm, the amplitude of the far-field pressure is smaller for all five observer positions. This could be attributed to the attenuation and spreading of the near-field pressure in the Vucalm calculation as it propagates across a coarser mesh in the region away from the bubble (mesh density reduces with increasing distance from the bubble). Another explanation for the difference could be attributed directly to the formulation of the FW-H code itself. As the integration surface is moved farther away, more of the nonlinearity contribution is accounted for by the surface integrals (di Francescantonio 1997; Brentner & Farassat 1998). Hence, the reduction in the amplitude of the far-field blast wave pressure might be because of the inclusion of higher degree of nonlinearity in the FW-H calculation. The nonlinearity causes steepening and shock dissipation. However, if this was the case, one would expect the difference between the two methods to be greater when $R_{cs} = 0.2$ mm. This is because the degree of nonlinearity is greater when $R_{cs} = 0.2$ mm than when $R_{cs} = 0.35$ mm. The Kirchhoff method is expected to be prone to error if the control surface is in the nonlinear region, but not the FW-H. However, the results presented here show that the Kirchhoff and FW-H methods agree well for $R_{cs} = 0.2$ mm. Therefore, it is unlikely that the discrepancy is due to the greater nonlinearity in the region where $R_{cs} = 0.2$ mm. Hence, the dissipation in the blast wave pressure for $R_{cs} = 0.35$ mm predicted by FW-H code is most probably due to coarsening of the Voronoi mesh in the region away from the bubble in the Vucalm simulation.

The predictions presented here are compromised by the assumption of linear propagation outside of the control surface, which introduces a degree of error that is yet unquantified. Here, we explore the nature of this error, and § 3.5 describes methods for predicting far-field acoustic emissions.

3.4. *Nonlinear wave propagation*

The preceding discussion illustrates the importance of determining the presence and effects of nonlinearity, since much of acoustical theory is linear, in that it assumes a linear relationship between acoustic pressure and density. This approximation can be thought of as neglecting the higher order terms in the following series expansion:

$$p = c_0^2 \rho + \frac{1}{2} \frac{c_0^2}{\rho_0} \frac{B}{A} \rho^2 + \cdots, \tag{3.2}$$

where c_0 is the sound speed for waves of infinitesimal amplitude and B/A is the second-order parameter of nonlinearity, and for water $B/A = 5$ (Leighton 2007).

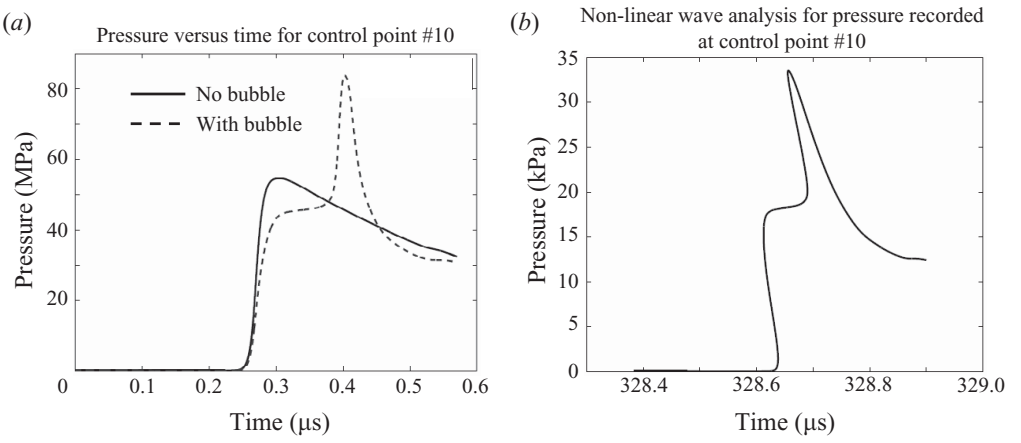

FIGURE 12. (*a*) The pressure-time history at the control point number 10, C^{10}_{axi} (see figure 7). (*b*) The effect of nonlinearity on the pressure amplitude and shape of the waveform shown in frame (*a*).

Nonlinear absorption is a process associated with nonlinear propagation that leads to a change in the amplitude and shape of the propagating wave. During nonlinear acoustic wave propagation, the higher order term pumps energy from lower to higher frequencies, and plane wave descriptions are available as to how the balance between this effect and absorption changes the waveform (Hamilton & Blackstock 1998; Leighton 2007). A method for transforming plane wave solutions to account for spreading of spherical waves is given by Hamilton & Blackstock (1998). The solution for the pressure of a spherical wave with source condition $p = f(t)$ at $r = r_0$ is given by

$$p(r, \tau) = \left(\frac{r_0}{r}\right) f\left(\tau \pm \left(\frac{\beta p r}{\rho_0 c_0^3}\right) \ln\left(\frac{r}{r_0}\right)\right), \tag{3.3}$$

where r is the radial coordinate (defined positive outward), ρ is the density, c is the sound speed, τ is the coordinate for the retarded time frame (i.e. $\tau = t \mp (r - r_0)/c_0$) and β is the traditional coefficient of nonlinearity for the fluid in which the wave propagates, given by $1 + B/(2A)$.

The pressure–time histories recorded at one of the control points (i.e. number 10, C^{10}_{axi}) on the control surface with and without the bubble present are depicted in figure 12(*a*). For simplicity, we ignore the pressure contribution from other control points. For any distance r, higher pressure values will travel faster than lower pressure values. As a result, at some propagation distance, the high-amplitude compressive pressure will overtake the lower pressure portion of the waveform. The effect of nonlinearity on the pressure plotted in figure 12(*a*) is given in figure 12(*b*). The solution is no longer valid because it predicts a multi-valued waveform, which is not physical.

The acoustic propagation to the far field using the Kirchhoff and FW-H methods were performed using linear wave propagation. Given the amplitudes and distances involved, some nonlinear propagation will have occurred, although more so in water than tissue because of the higher absorption in the latter – see (§ 3.5). The validation exercise undertaken for both the Kirchhoff and FW-H codes (§ 2.2.3) did not test the effect of nonlinear propagation: an analytical solution was used to provide the data

on the control surface, and then these data were used as inputs to the Kirchhoff and FW-H codes to estimate the far-field pressure emission and compare that with the analytical solution. The distance of the control surface for the validation exercise was 10 times the equilibrium radius of the pulsator, whilst in the far-field calculations presented for SWL (figures 11 and 18) the control surface is only five times the initial bubble radius. The obvious solution would be to compute the flow field out to ranges sufficient to ensure negligible nonlinear propagation, but this was not feasible with the computational facilities available for the studentship reported here. A lower cost option is to estimate the effect of nonlinear propagation by analysing the nonlinear spherical wave propagation shown in figure 12(*b*). It is clear that the solution predicts a multi-valued waveform. In order to avoid unphysical solutions, the wave should be propagated in small steps. Each time the wave tends to become multi-valued, the multi-valued region should be replaced with a shock front using the equal area rule (see Hamilton & Blackstock 1998, p. 102). The shock is then propagated at the mean of the two velocities appropriate to the pressures either side of the shock front. This is a weak shock model.

To summarize, there are two options for correcting the far-field predictions in § 3.3 for the omission of nonlinear propagation outside of the control surface. Such propagation undoubtedly occurs, given amplitudes of 80 MPa on the control surface shown in figure 12(*a*). One is to use a sufficiently (but currently unfeasible) large control surface such that all the nonlinear propagation takes within it. The second is to use the method of § 3.4 to propagate waveforms in the manner of (3.3) from one control volume to a larger one, then use these waveforms as input for a new FW-H prediction based on this larger control surface and using successive control surfaces until such distances are achieved that the dynamics are sufficiently linear.

However, both approaches are prohibitively computationally expensive for the resources of this project. A more important feature is to consider the effect of real tissue, given that the Vucalm simulations assumed water around the bubble. An objective of this project was to understand the sources of, and trends in, the far-field characteristics to allow estimation of the extent to which the predictions of the Gilmore model could be trusted. This was important because although the Gilmore model contains assumptions that would not be met in practice (the bubble remains spherical and intact at all times and pulsates in an infinite homogeneous body of liquid), its computational speed in obtaining far-field predictions was faster than the approach described in this paper, and so (once its limitation had been characterized against test cases using Vucalm) the Gilmore model was sufficiently rapid to cover the great variety of clinical conditions needed for the development of the device. Therefore, we will next consider the extent to which the presence of tissue, as opposed to water, affects the far-field waveforms.

3.5. *The effect of tissue*

The cavitation detected by the clinical sensor occurs, not in water, but *in vivo*. Whilst *in vivo* cavitation can differ greatly from that in water if, for example, the bubble is confined within a blood vessel (Leighton, White & Marsden 1995*a*, *b*; Zhong *et al.* 2001; Cui *et al.* 2006; Gao, Hu & Hu 2007; Sassaroli & Hynynen 2007; Freund 2008), the cavitation simulated for this model resembles more that undertaken in the urine collection system, where cavitation is known to occur more readily during SWL than it does in the parenchyma (Bailey *et al.* 2005). However, the subsequent propagation of the acoustic wave occurs through a variety of other tissue types that can differ significantly from water in the extent to which they tend to promote nonlinear

propagation (through B/A) and the extent to which the waves (and particularly any higher harmonics) are suppressed through frequency-dependent absorption. The balance between the two is characterized by the Gol'dberg number, equal to the ratio of the two length scales. It is given by the e-folding distance for the amplitudes of acoustic pressure to be absorbed, divided by the propagation distance required to form a shock through nonlinear propagation in the absence of absorption. Hence, the Gol'dberg number is greater than unity if nonlinear effects dominate, and less than unity if the absorption (which tends to increase with frequency) dominates over and above the tendency to propagate nonlinearly (Gol'dberg 1956; Leighton 2007). Its value depends on the signal amplitude, frequency content and the tissue medium: in urine it tends to be high because of low absorption, whereas in fat it tends to be less than unity because of high absorption there (Bouakaz *et al.* 2004).

The authors could find no information for the clinical scenario they consider, of a spherically spreading blast wave of more than 1 GPa peak overpressure, the Gol'dberg numbers for tissue having been characterized for plane wave propagation of pressure fields with amplitudes typical of those generated directly by clinical diagnostic apparatus (Haran & Cook 1983; Duck 2010). In general, B/A varies only by a factor of around 2 between tissue types for a beam of given amplitude, being similar to water for most liquid tissues like urine, and ranging up to double that of water for fat. This is very much less than the range seen in absorption between various tissues. Hence, in translating the nonlinearity propagation seen in water to that seen in tissue for the same beam, for most tissue types it is the change in absorption which is the overwhelming consideration, not the change in B/A (Duck 2010). The absorption coefficients for soft tissue in the literature are for lower signal amplitudes than the $\sim$1 GPa levels found in this paper, and vary considerably (Burley *et al.* 1980; Goss, Johnston & Dunn 1980; Damianou, Sanghvi & Fry 1997; Bailey *et al.* 2003; Zderic *et al.* 2004; Liu *et al.* 2006; Coussios & Roy 2008). To reduce the range of values available even for the restricted amplitude range of clinical diagnostic device output, it is a standard practice to 'derate' the field values measured in water by $0.3\,\mathrm{dB\,cm^{-1}\,MHz^{-1}}$, and for the data specific to the tissues and amplitudes occurring in this paper, this is also applied to the predicted values here to estimate the signals that would be detected were the fields to propagate through soft tissue. The authors recognize that, in the absence of accepted procedures for higher amplitudes, they are applying the derating rules outside of the amplitude range for which they were intended.

Even though there are some features that will mitigate the assumptions compromised in using this standard value (e.g. the spherical spreading of the blast wave will rapidly attenuate it), nevertheless it is recognized that data for the specific conditions of the pressure field and tissue relevant to this paper are required, but not currently available. Applying this correction to the Fourier transforms of the data in figure 11(*c*) (and, later, figure 18*b*), and then performing an inverse Fourier transform, therefore provides the best estimate currently available for the far-field waveform that would be detected through tissue. Figure 11(*d*) shows the data of figure 11(*c*) but derated by the standard value of $0.3\,\mathrm{dB\,cm^{-1}\,MHz^{-1}}$ to include the effect of absorption in tissue. This reduces the amplitudes significantly; the various peaks are more severely attenuated as the characteristic frequencies increase (such that the second maximum at 90° is significantly attenuated between figures 11*c* and 11*d*). The attenuation was included by taking a fast Fourier transform (FFT) of the data, applying the filter and then applying an inverse-FFT. This method provides a conservative estimate since such a correction does not allow for the extra absorption

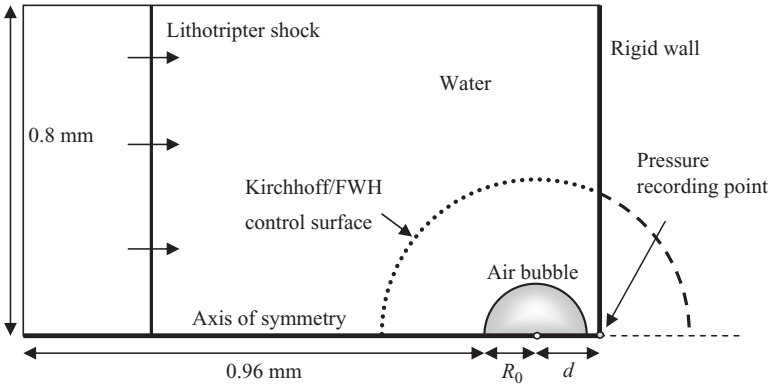

FIGURE 13. A bubble ($R_0 = 0.04$ mm) initially located at a distance d near a rigid wall interacts with a lithotripter shock ($P^+ = 60$ MPa, $P^- = -10$ MPa). The Kirchhoff/FW-H control surface has a radius $R_{cs} = 5\,R_0 = 0.2$ mm and 90 control points. Only the control points inside the domain (dotted line) contribute to the far-field acoustic emission calculation. Figure not to scale.

that is caused by nonlinear propagation (Liu *et al.* 2006). It is applied here because application of such linear correction factors is currently the standard method of correcting in-water measurements of sound fields for *in vivo* ones, and indeed much of the safety procedures for biomedical ultrasound are based on such a methodology (O'Brien, Yang & Simpson 2004; Whittingham 2007).

4. Lithotripter shock–bubble interaction near a rigid wall

Simulations of single bubble collapses near a rigid wall at various stand-off distances are presented here. The aims are to study the interaction phenomena, the collapse of the bubble, the effects of stand-off distances ζ and the far-field acoustic emissions from the cavitation events evaluated using the Kirchhoff and FW-H schemes. The schematic of the interaction is illustrated in figure 13. The initial conditions of the flow are given in table 1, and $R_0 = 0.04$ mm (Cunningham *et al.* 2001). Approximately 3.5×10^4 cells were used, and all elapsed times are measured from when the shock first impacts the bubble. The observer is placed at a distance $r_b = 150$ mm from the initial bubble centre at five different locations on the XY-plane.

Six different simulations presented here are based on the stand-off distances, ζ, listed in table 2. The lithotripter shock strength and initial bubble radius are constant, but the distance d varies. For calculation of ζ, the bubble maximum radius, R_{max}, is taken to be the bubble initial radius, R_0. This assumes that, before it is collapsed by the lithotripter shock, the bubble is at its maximum radius. Here, the asymmetric collapse of the bubble is induced not only by the relatively strong lithotripter shock but also by the presence of the rigid wall.

4.1. *Detailed analysis of the bubble with* $\zeta = 1.0625$

The interaction of the shock with this bubble is chronologically shown in figure 14. The transmitted shock inside the bubble induces substantial heating of the content of the bubble (assumed to be air) (Ball *et al.* 2000). The bubble undergoes a violent deformation that includes high-speed jet impingement, shock transmission and reflection, blast wave emission from the jet impact and bubble fragmentation, which are similar to those of the interaction in a free field (§ 3.2).

Case	Initial radius R_0 (μm)	Distance d (μm)	Stand-off distance ζ
1	40	42.5	1.0625
2	40	45.0	1.125
3	40	55.0	1.375
4	40	65.0	1.625
5	40	75.0	1.875
6	40	85.0	2.125

TABLE 2. Six case studies are simulated for a bubble collapse near a rigid wall. The stand-off distance $\zeta = d/R_{max}$, where the bubble maximum radius, R_{max}, is here taken to equal R_0.

At $t = 0.06\,\mu s$, the incident shock has traversed the full bubble width and impacts the wall (figure 14*b*). The reflected shock further interacts with the expansion wave (figure 14*c*), but the bubble's downstream surface is minimally affected by the shock. This results in the non-symmetric deformation of the bubble whereby the upstream surface moves rapidly to the right but the downstream surface remains static. The reflected incident shock impacts the downstream surface creating a high-pressure region above the bubble, which appears to compress the bubble (figure 14*d*). A steep pressure gradient in the water near the left side of the bubble drives the flow creating the impinging jet (figure 14*d–f*).

The initially weak transmitted shock propagating within the bubble has strengthened as a result of the focusing effect arising from the curvature of the bubble interface (figure 14*d*). By $t = 0.14\,\mu s$, the shock within the bubble converges near the bubble downstream surface and results in an increase in pressure in that region. The intricate shape of the transmitted shock is a consequence of both the geometry of the bubble surface that confines the shock and the variation of the geometry with time. Moreover, the spatially non-uniform deformation of the bubble surface yields a higher water velocity on the bubble centreline. This, in turn, generates additional compression waves in the air near the bubble's upstream surface, which strengthen the transmitted shock (figure 14*g–j*).

At $t = 0.184\,\mu s$, the bubble upstream surface has fully formed the high-speed jet that accelerates towards the wall. The water layer trapped between the bubble and the wall appears to stagnate. The slight bubble elongation in the axial direction is due to its interaction with the reflected incident shock that contracts the top bubble surface. This deformation is not seen in the free field scenario. Another feature that differs from the free field scenario is the shape of the liquid jet tip. There appears to be a slight indentation on the jet tip on the symmetry axis. The tip is not perpendicular to the symmetry axis as depicted in the close-up view of figure 14(*g*), and therefore its leading annular front will actually impact the downstream surface earlier than its centreline. This slightly concave shape is thought to be caused by a recirculating flow at the tip of the jet, induced near the bubble upstream surface from the interaction of the reflected incident shock with the strong expansion wave originating from the bubble surface. This may trap gas that will be compressed during jet impact, and explain some observations of luminescence from the jet tip (Bourne & Field 1991; Leighton 1994; Bourne & Milne 2003) shortly before luminescence is detected from the gas compressed in the toroid.

Furthermore, as the jet propagates, compression waves are generated in the bubble, which in figure 14(*g*) are indicated by a secondary shock moving to the right. The

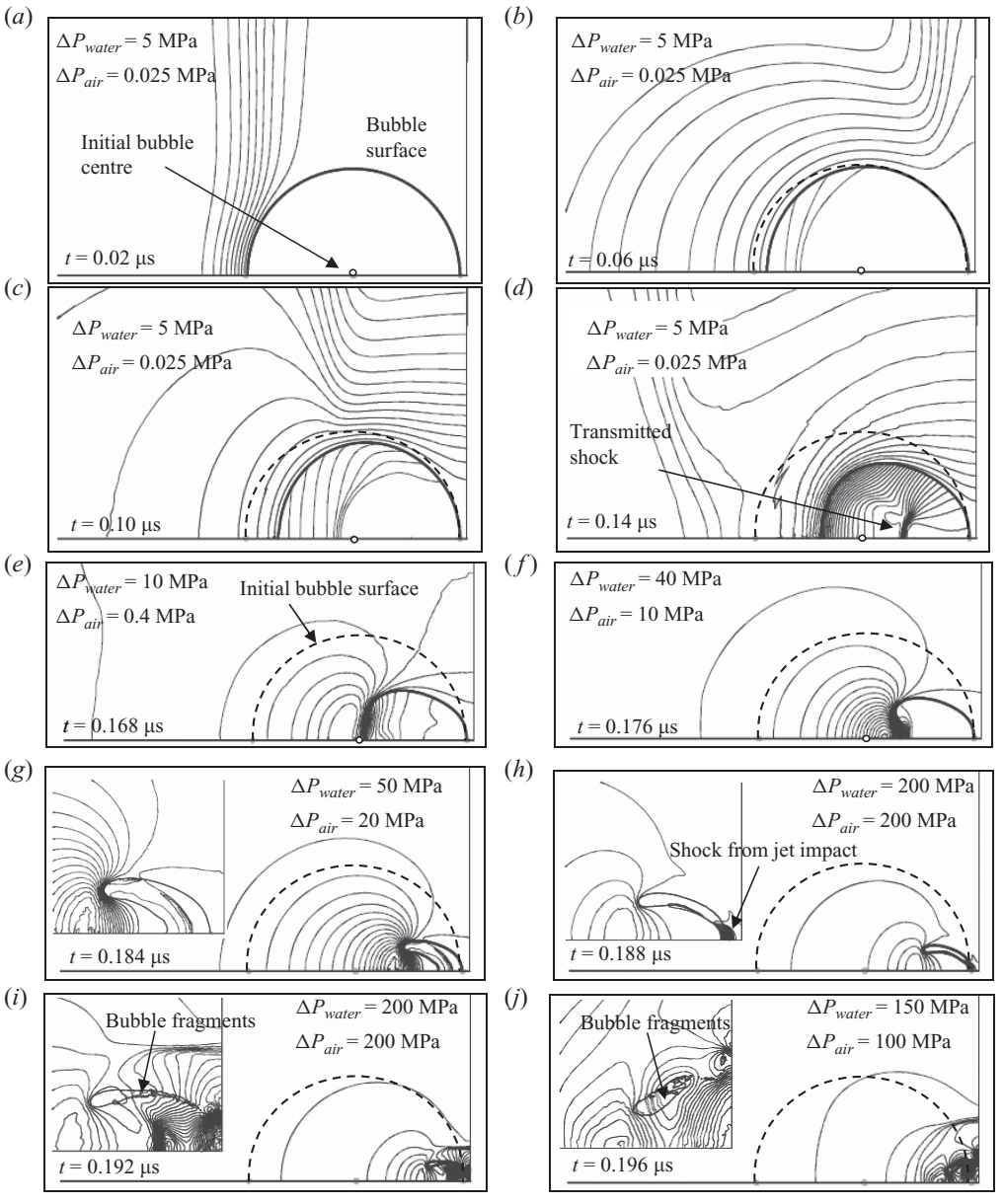

FIGURE 14. Plots of pressure contours (*a*)–(*j*) of a bubble ($R_0 = 1.5\,\mu$m) collapsed by a lithotripter pulse ($P^+ = 60$ MPa). The stand-off parameter $\zeta = 1.0625$. Insets are close-up views.

strength of this secondary shock increases and it eventually impacts the bubble downstream surface. This impact precedes the impact of the jet on to the downstream surface although both occur within a very short time span (figure 14*g*). When the jet eventually impacts the downstream surface, an intense blast wave is emitted to the surrounding water (figure 14*h*). This wave eventually combines with the one from the secondary shock impact. At $t = 0.192\,\mu$s, the jet has penetrated through the bubble, isolating a toroid of trapped and highly compressed air (figures 14*i*) and is

followed by bubble fragmentation. Although this fragmentation appears physically plausible, it is very difficult to quantify experimentally owing to the physical size of the fragments and time scale of the problem. If such tiny isolated islands of air do exist, they may coalesce with the main cavity as the flow evolves or act as nuclei for further cavitation events. The interaction of these nuclei with the tensile part of the lithotripter shock wave may also cause them to expand and later collapse, either spherically or non-spherically depending on the nature of the flow around the bubble and the influence of nearby rigid walls. The bubble fragments could also be collapsed by shock waves emitted from the collapse of neighbouring bubbles.

The interaction between the high-momentum liquid jet and the downstream low-momentum water produces a strong vortex flow. The flow is also redirected along the wall. As a result of the high velocity of the jet, the blast wave advances relatively slowly to the left along the symmetry axis (figures 14*i*). The blast wavefront propagating to the right impacts the rigid wall and is reflected back into the surrounding water. Part of this wave will interact with the remaining cavity. The air cavity and the bubble fragments are then drawn into the vortex core bringing them even closer to the wall (figures 14*j*). The regrowth and collapse of this air cavity is expected to cause further damage to the wall as also identified by Shima (1997).

The damage pattern arising from these impulsive pressure and jet impingement and bubble fragments has been observed on a 0.02 mm thick aluminium foil (Coleman *et al.* 1987) and an indium specimen (Tomita & Shima 1986). The regrowth of the cavity occurs soon after the jet impact when the air inside the bubble becomes highly compressed. Regrowth would occur even in the absence of the tensile tail of the liquid. If, say the static pressure in the liquid were 1 bar, the high pressure in the compressed gas at the end of the collapse would cause the bubble to grow to volumes where the internal pressure is much less than 1 bar because, as it passes through a size when its internal pressure resembles 1 bar, it continues to grow as a result of the inertia of the surrounding liquid. However, in the case of SWL, the liquid will be driven by the tensile tail of the lithotripter pulses, and this will dominate the growth (Leighton & Cleveland 2010). Once the bubble growth has ceased, a collapse will follow.

4.2. *Effects of stand-off distance, ζ, on bubble behaviour*

Plots of time histories of bubble surface velocities, bubble volume and pressure loading on the rigid wall for different ζ are shown in figure 15. The bubble upstream surface forms the high-speed jet. The velocities of both upstream and downstream surfaces show an increase towards the end of the collapse (figure 15*a*). However, the plots indicate a transition associated with ζ at which the influence of the rigid wall on the collapse is significant. For the upstream surface (jet), the curves of $\zeta = 1.0625$ and $\zeta = 1.125$ can be distinguished from the others where ζ are relatively larger. They show that after $t = 0.15\,\mu$s the jet velocity increases dramatically as it approaches the downstream surface, whereas for cases 3–6 the increase is only gradual. Also, for cases 1 and 2, the jet velocity reaches over $2\,\mathrm{km\,s^{-1}}$ compared to less than $1\,\mathrm{km\,s^{-1}}$ for cases 3–6. For the downstream surface velocity, the trend is reversed. The surface velocity of cases 3–6 increases gradually to about $250\,\mathrm{m\,s^{-1}}$, but to only less than $100\,\mathrm{m\,s^{-1}}$ for cases 1 and 2. This correlates with the highly non-spherical collapse phenomenon where the downstream surface is shielded from the oncoming incident shock when the bubble is very close to the wall.

Figure 15(*b*) shows the effect of varying ζ on the bubble volume (normalized by the initial volume, V_i). It shows a nearly linear volume reduction from $t \simeq 0.1\,\mu$s to

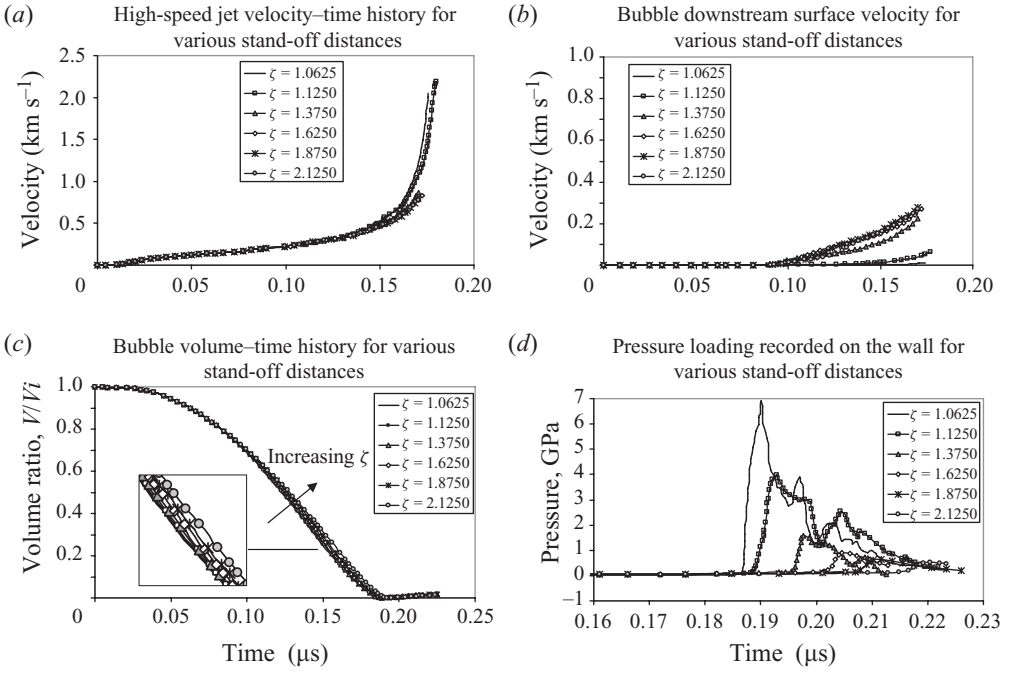

FIGURE 15. Detached bubble. Comparison for different stand-off distances, ζ (table 2): (*a*) High speed jet (bubble upstream surface) velocity–time history, (*b*) bubble downstream surface velocity–time history, (*c*) bubble volume–time history, (*d*) pressure loading–time history recorded on the rigid wall.

$t \simeq 0.17\,\mu s$ where it falls from about 0.70 to 0.15. This near-linear phase ends as the jet approaches the downstream surface. After the jet impact, the volume continues to decline, reaching a minimum at $t \simeq 0.18\,\mu s$ before the bubble enters the vortex core and begins to expand. The curves also indicate a trend of increasing bubble collapse rate for decreasing ζ. One might expect that the collapse rate for cases 3–6 should be higher than that of cases 1 and 2 due to the fact that the bubble surface contraction occurs in all directions. However, the deformation of the upstream surface that manifests into a high-speed jet compensates for the small contraction rate of the downstream surface in cases 1 and 2 and therefore, the collapse rate is greater as ζ decreases. The figure also suggests that the time for the bubble to reach minimum volume increases with increasing ζ. In contrast to the free field case ($\zeta = \infty$) where the bubble does not experience a lateral compression, in the case when the bubble is near a rigid wall, the interaction with the reflected incident shock provides a lateral compression to the collapsing bubble. This collapse is also more violent as the jet velocity exceeds $2\,km\,s^{-1}$ for $\zeta = 1.0625$, and only up to approximately $1.3\,km\,s^{-1}$ for $\zeta = \infty$.

The pressure–time histories recorded on the rigid wall (figure 15*c*) suggest that the peak pressure corresponds to the blast wave emitted by the jet impact (liquid–liquid impact). The pressure associated with the incident shock is not registered because the wall is shielded by the bubble. The peak pressure recorded on the wall drops when ζ increases (increased distance) because the blast wave that propagates nearly spherically attenuates approximately in proportion to $1/r^2$. Following the sharp

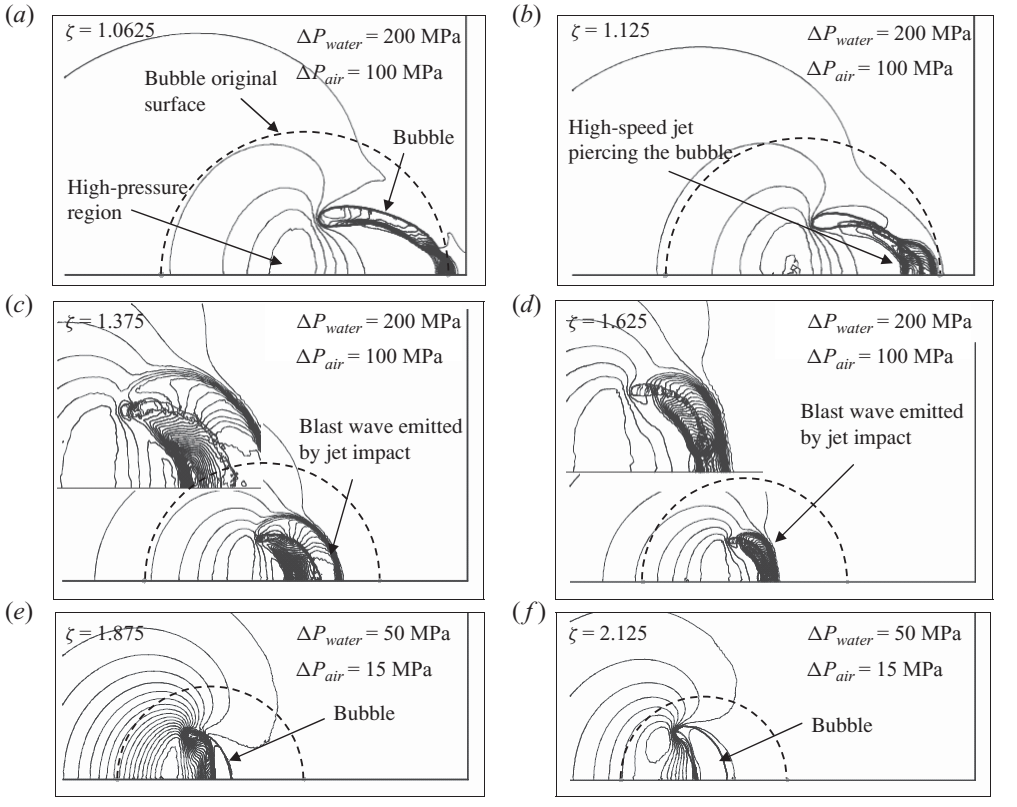

FIGURE 16. Plots (*a*)–(*f*) of pressure contours at $t = 0.188\,\mu$s after the shock hits the bubble. Comparison of bubble dynamics when the jet impacts the bubble's opposite wall for various stand-off parameters ζ. Bubble initial radius, $R_0 = 40\,\mu$m, and lithotripter shock strength $P^+ = 60$ MPa. The dashed line indicates the original bubble shape and location.

pressure peak, two other peaks can be observed for $\zeta = 1.0625$, 1.125 and 1.375. The first one is generated by the large dynamic pressure of the high-speed jet as it hits the wall. The second is dominated by pressure emitted from the bubble rebound, but its amplitude is much lower than the other two peaks. The maximum pressure recorded varies from nearly 7 GPa for $\zeta = 1.0625$ to a mere 0.5 GPa for $\zeta = 2.125$. It would be a likely candidate to assess for the generation of at least surface damage on a nearby surface, although full assessment of all possible contributions to damage is beyond the scope of this article (Philipp & Lauterborn 1998; Tong *et al.* 1999; Eisenmenger 2001; Zhong *et al.* 2001; Zhu *et al.* 2002; Cleveland & Sapozhnikov 2005; Birkin *et al.* 2005*a*; Calvisi *et al.* 2007, 2008; Klaseboer *et al.* 2007; Sapozhnikov *et al.* 2007; Iloreta *et al.* 2008; Lauterborn & Kurz 2010; Vian *et al.* 2010).

Comparisons of the bubble behaviour for various ζ during the jet impact and the blast wave emission from the impact are depicted in figures 16 and 17 for $t = 0.188\,\mu$s and $t = 0.2\,\mu$s, respectively. One obvious difference is the shape of the bubble. For bubbles with small ζ, elongation is due to the more profound influence of the rigid wall compared to those with larger ζ. This agrees with the earlier discussion that the bubble behaviour for various ζ studied here shows two different trends, and that a transition point for ζ that reflects the asymmetry effect of the wall lies somewhere

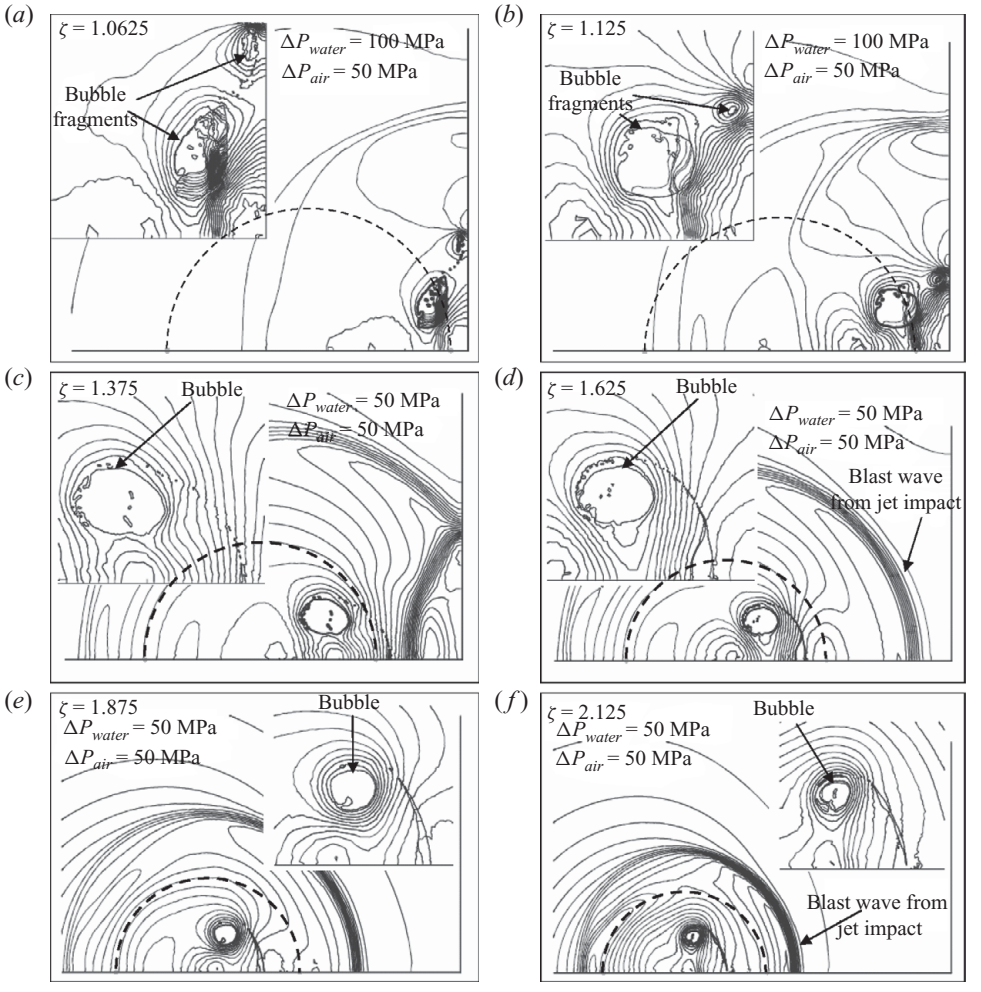

FIGURE 17. Plots (*a*)–(*f*) of pressure contours at $t = 0.2\,\mu$s after the shock hits the bubble. Comparison of bubble dynamics after the jet impact for various stand-off parameters ζ, showing an intense blast wave emission. $R_0 = 40\,\mu$m and $P^+ = 60$ MPa. The dashed line indicates the original bubble shape and location. Insets are close-up views.

between 1.125 and 1.375. Below this ζ, the contributory effect from the wall is significant.

The shape of the jet is narrower in cases 1 and 2 (due to the elongation of the collapsing bubble associated with its interaction with the reflected incident shock) than in cases 3–6 where the 'shoulder' of the jet is broader (figure 16). The circulating flow near the bubble's upstream surface creates a concave jet tip, which is highly prominent for $\zeta = 1.375$ and $\zeta = 1.625$. The jet tip is relatively wide and much flatter in cases 5 and 6.

The moment after the jet impact is shown in figure 17. For cases 1 and 2, the jet has penetrated through the bubble isolating a few toroidal bubble fragments (figure 17*a*, *b*). In cases 3–6, as a result of the highly concave jet, the impact of the jet on the downstream surface forms a toroidal bubble of highly compressed air and tiny bubble fragments (figure 17*c*–*f*) originating from the air layer trapped

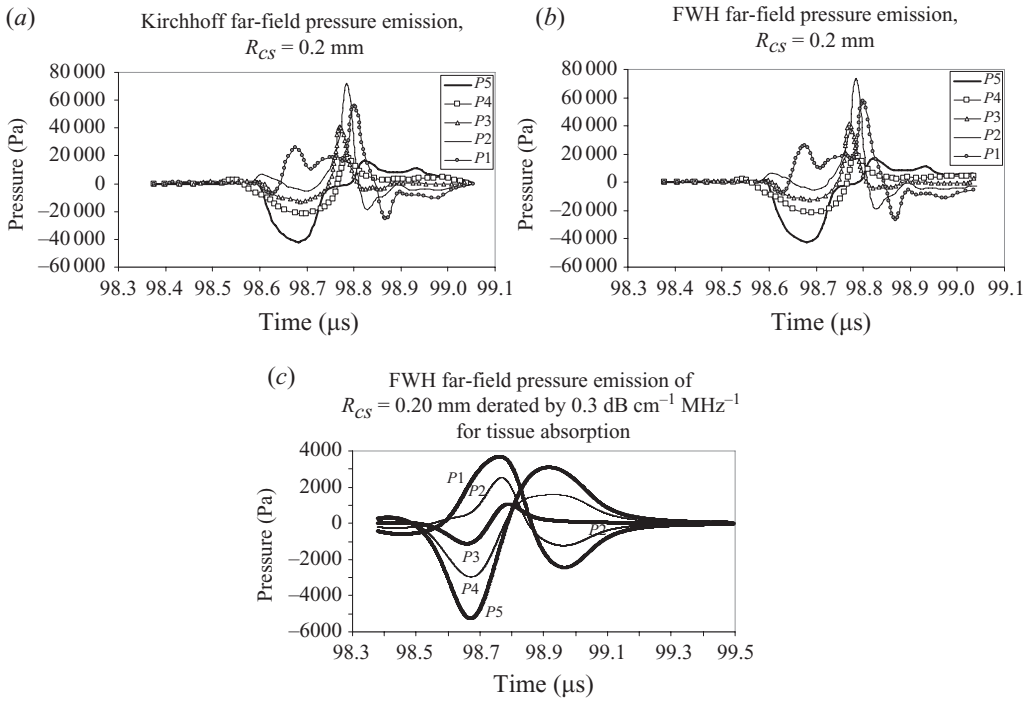

FIGURE 18. The far-field acoustic emissions read by an observer located at 150 mm from the initial bubble centre for five θ and ϕ combinations (i.e. observer's locations denoted by P1–P5 – refer to figure 10). (*a*) Kirchhoff scheme, (*b*) FW-H scheme. Stand-off distance $\zeta = 1.0625$ and control surface radius $R_{cs} = 0.2$ mm, (*c*) The data of frame (*b*) derated by the standard value of 0.3 dB cm^{-1} MHz^{-1} to include the effect of absorption in tissue.

between the jet and the downstream interface prior to impact. Of course, under such extreme conditions, the details of the air/water interfaces must be treated with caution, although such predictions are in keeping with experimental observations such as the observation of damage rings around jet impact damage pits (Philipp & Lauterborn 1998) and luminescence at the point of jet impact (Bourne & Field 1991; Leighton 1994; Bourne & Milne 2003).

4.3. *Far-field acoustic emissions of bubble collapse near a rigid wall*

Figure 18 shows the pressure–time history calculated in the far field for $\zeta = 1.0625$ using the Kirchhoff and FW-H schemes. Results for five different combinations of θ and ϕ are plotted for comparison in order to determine the variation in the far-field pressure profile at different observer positions and the dependency on the directionality of the lithotripter shock wave. The same set of integration surfaces and input data from Vucalm simulations were used for all calculations.

For the case when the rigid wall is present, the incident shock passes twice over the bubble (once travelling from left to right, and then as a reflected wave travelling from right to left). Therefore, pressure waves directly related to the propagating incident shock are captured twice in the Kirchhoff and FW-H surface integral. Nevertheless, the blast wave could still be captured as a sharp peak. The timing of the arrival of the blast wave peak relative to the contamination from the lithotripter shock is such that there is no overlap. Jamaluddin (2005) demonstrated that the blast wave can be unambiguously identified from the lithotripter signature by comparing the

far-field pressure waveforms for the bubble-free cases with those when bubbles are present. In figure 18, the large trough for $\zeta = 1.0625$ (P5 line) between 98.6 and 98.75 μs can be attributed to the incident shock. The maximum pressure amplitude predicted for $\zeta = 1.0625$ is approximately 70 kPa. This value decreases by around 10 kPa when $\zeta = 2.125$. The reduction in the maximum pressure amplitude is because of the increase in the distance from the wall of the initial position of the bubble centre. For $\zeta = 1.0625$, the reflection of the blast wave is not very clear. This is because the delay between the primary and reflected shocks may be too small to resolve. For $\zeta = 2.125$, Jamaluddin (2005) shows that the acoustic emission curve depicts the second pressure peak owing to the greater distance of the bubble from the rigid wall, and that the blast wave has time to develop into a full spherical pressure wave and is reflected by the wall.

The results of the predicted far-field acoustic emission using the FW-H method are in agreement with that of the Kirchhoff method (figure 18*a*, *b*) for all five observer positions. This particular problem has a high degree of flow nonlinearity at any feasible position of the control surface owing to the incident shock wave, its reflection by the rigid wall and the high pressure amplitude of the blast wave. As the FW-H formulation takes into account the flow nonlinearities in the surface integrals, the FW-H method is expected to give more consistent and acceptable results regardless of the control surface position compared to the Kirchhoff method. The results show that there are negligible differences in the abilities of both methods to distinguish the lithotripter signature from the blast wave signature. Therefore, the implementation of both methods warrants exploration in this particular scenario.

Figure 18(*c*) shows derated versions of the data in figure 18(*b*) to include the effect of absorption in tissue (as was done to generate figure 11*d*). The divergence on the left of the figure is an artefact. It is not a frequency folding effect (it does not, for example, occur at the extreme right of the plots) but instead occurs because the derating algorithm is defined in terms of amplitude alone, at $0.3\,\mathrm{dB\,cm^{-1}\,MHz^{-1}}$. For want of information to the contrary, a zero-phase response is included with the filter (i.e. a filter that introduces no delays). Such filters are acausal, in that they create an output using data before and after the current sample, which produces an unphysical result in this case. However, application of an acausal filter in this way is deemed here to be an appropriate procedure to obtain an estimate of the effect of tissue absorption, in the absence of specific information on the phase requirements of the filter. Whilst this effect would in principle have occurred in figure 11(*d*), the nature of the signal made it undiscernible.

5. Conclusions

The jetting collapse of a single bubble in a free field and near a rigid wall for various stand-off distances due to interaction with a lithotripter shock has been simulated using the FLM code. The collapse is asymmetric, forming a high speed jet that impacts the far bubble wall, generating an intense blast wave. To predict the far-field acoustic emissions from the bubble collapse, the time histories of pressure and its derivatives recorded on a control surface placed inside the FLM computational domain are used as inputs to the Kirchhoff and FW-H methods. For the control surface radii employed here ($R_{cs} = 5\,R_0 = 0.2$ mm for an initial bubble radius of $R_0 = 40\,\mu$m), both methods are able to predict the far-field acoustic emissions in water. However, the method is only accurate if the control surface is placed at a sufficient range from the source

to ensure that only linear acoustic propagation occurs beyond it; if the CFD field is too limited for this, an alternative method of nonlinearly propagating the waveform between increasingly large control surfaces should be considered. In the current project studentship, the computational resources were insufficient to implement either approach. However, the scenario of interest here is to support understanding of a clinical device, and the importance of balancing the tendency of tissue to generate nonlinear waveforms with its ability to absorb the waveform was outlined, and the waveforms corrected following the standard derating procedure which neglects the effects of nonlinear propagation. Having demonstrated the technique for predicting the acoustic emission from single bubbles, the next paper in this series will show how this is developed to predict the far-field acoustic emissions from single bubbles attached to a wall and from cavitation clouds during SWL.

A. R. Jamaluddin was supported through a PhD studentship provided by the EPSRC (grant no. *GR/N*19243; Principal Investigator: T. G. Leighton). The authors are grateful to Prof. P. White for assistance in producing the derated values in figures 11(*d*) and 18(*c*).

REFERENCES

Bailey, M. R., Khokhlova, V. A., Sapozhnikov, O. A., Kargl, S. G. & Crum, L. A. 2003 Physical mechanisms of the therapeutic effect of ultrasound (a review). *Acoust. Phys.* **49** (4), 369–388.

Bailey, M. R., Pishchalnikov, Y. A., Sapozhnikov, O. A., Cleveland, R. O., McAteer, J. A., Miller, N. A., Pishchalnikova, I. V., Connors, B. A., Crum, L. A. & Evan, A. P. 2005 Cavitation detection during shock-wave lithotripsy. *Ultrasound Med. Biol.* **31** (9), 1245–1256.

Ball, G. J. 1996 A free-Lagrange method for unsteady compressible flow: simulation of a confined cylindrical blast wave. *Shock Waves* **5**, 311–325.

Ball, G. J., Howell, B. P., Leighton, T. G. & Schofield, M. J. 2000 Shock-induced collapse of a cylindrical air cavity in water: a free-Lagrange simulation. *Shock Waves* **10**, 265–276.

Benjamin, T. B. & Ellis, A. T. 1966 The collapse of cavitation bubbles and the pressure thereby produced against solid boundaries. *Phil. Trans. R. Soc. Lond.* A **260**, 221–240.

Birkin, P. R., Offin, D. G., Joseph, P. F. & Leighton, T. G. 2005*a* Cavitation, shock waves and the invasive nature of sonoelectrochemistry. *J. Phys. Chem.* B **109**, 16997–17005.

Birkin, P. R., Offin, D. G. & Leighton, T. G. 2004*a* Electrochemical measurements of the effects of inertial acoustic cavitation by means of a novel dual microelectrode. *Electrochem. Commun.* **6** (11), 1174–1179.

Birkin, P. R., Offin, D. G. & Leighton, T. G. 2004*b* The study of surface processes under electrochemical control in the presence of inertial cavitation. *Wear* **258** (1–4), 623–628.

Birkin, P. R., Offin, D. G. & Leighton, T. G. 2005*b* Experimental and theoretical characterisation of sonochemical cells. Part 2. Cell disruptors (ultrasonic horn) and cavity cluster. *J. Phys. Chem.* **7**, 530–537.

Blake, J. R., Hooton, M. C., Robinson, P. B. & Tong, R. P. 1997 Collapsing cavities, toroidal bubbles and jet impact. *Phil. Trans. R. Soc. Lond.* A **355**, 537–550.

Blake, J. R., Taib, B. B. & Doherty, G. 1986 Transient cavities near boundaries: Part 1. Rigid boundary. *J. Fluid Mech.* **170**, 479–497.

Bouakaz, A., Merks, E., Lance'e, C. & Bom, N. 2004 Noninvasive bladder volume measurements based on nonlinear wave distortion. *Ultrasound Med. Biol.* **30** (4), 469–476.

Bourne, N. K. & Field, J. E. 1991 Bubble collapse and the initiation of explosion. *Proc. R. Soc. Lond.* A **435**, 423–435.

Bourne, N. K. & Field, J. E. 1999 Shock-induced collapse and luminescence by cavities. *Proc. R. Soc. Lond.* A **357**, 295–311.

Bourne, N. K. & Milne, A. M. 2003 The temperature of shock-collapsed cavity. *Proc. R. Soc. Lond.* A **459**, 1851–1861.

Brentner, K. S. & Farassat, F. 1998 Analytical comparison of the acoustic analogy and Kirchhoff formulation for moving surfaces. *AIAA* **36** (8), 1379–1386.

Brujan, E. A., Nahen, K., Schmidt, P. & Vogel, A. 2001 Dynamics of laser-induced cavitation bubbles near elastic boundaries: influence of the elastic modulus. *J. Fluid. Mech.* **433**, 283–314.

Burley, M. M., Madsen, E. L., Zagzebski, J. A., Banjavic, R. A. & Sum, S. W. 1980 A new ultrasound tissue-equivalent material. *Radiology* **134**, 517–520.

Calvisi, M. L., Iloreta, J. I. & Szeri, A. J. 2008 Dynamics of bubbles near a rigid surface subjected to a lithotripter shock wave. Part 2. Reflected shock intensifies nonspherical cavitation collapse. *J. Fluid. Mech.* **616**, 63–97.

Calvisi, M. L., Lindau, O., Blake, J. R. & Szeri, A. J. 2007 Shape stability and violent collapse of microbubbles in acoustic traveling waves. *Phys. Fluids* **19**, 047101.

Chaudhri, M. M. & Field, J. E. 1974 The role of rapidly compressed gas pockets in the initiation of condensed explosives. *Proc. R. Soc. Lond.* A **340**, 113–128.

Church, C. C. 1989 A theoretical study of cavitation generated by an extracorporeal shock wave lithotripter. *J. Acoust. Soc. Am.* **86**, 215–227.

Cleveland, R. O. & Sapozhnikov, O. A. 2005 Modelling elastic wave propagation in kidney stones with application to shock wave lithotripsy. *J. Acoust. Soc. Am.* **118** (4), 2667–2676.

Cleveland, R. O., Sapozhnikov, O. A., Bailey, M. R. & Crum, L. A. 2000 A dual passive cavitation detector for localized detection of lithotripsy-induced cavitation *in vitro*. *J. Acoust. Soc. Am.* **107**, 1745–1758.

Coleman, A. J., Choi, M. J., Saunders, J. E. & Leighton, T. G. 1992 Acoustic emission and sonoluminescence due to cavitation at the beam focus of an electrohydraulic shock wave lithotripter. *Ultrasound Med. Biol.* **18**, 267–281.

Coleman, A. J. & Saunders, J. E. 1989 A survey of the acoustic output of commercial extracorporeal shock wave lithotripters. *Ultrasound Med. Biol.* **15**, 213–227.

Coleman, A. J., Saunders, J. E., Crum, L. A. & Dyson, M. 1987 Acoustic cavitation generated by an extracorporeal shock-wave lithotripter. *Ultrasound Med. Biol.* **13**, 69–76.

Coleman, A. J., Whitlock, M., Leighton, T. G. & Saunders, J. E. 1993 The spatial distribution of cavitation induced acoustic emission, sonoluminescence and cell lysis in the field of a shock wave lithotripter. *Phys. Med. Biol.* **38**, 1545–1560.

Coley, G. D. & Field, J. E. 1973 The role of cavities in the initiation and growth of explosion in liquids. *Proc. R. Soc. Lond.* A **335**, 67–86.

Cooter, R. D., Babidge, W. J., Mutimer, K., Wickham, P., Robinson, D., Kiroff, G., Chapman, A. & Madden, G. J. 2001 Ultrasound-assisted lipoplasty. *Austral. NZ J. Surg.* **71** (5), 309–317.

Coussios, C. C. & Roy, R. A. 2008 Applications of acoustics and cavitation to noninvasive therapy and drug delivery. *Annu. Rev. Fluid Mech.* **40**, 395–420.

Cui, J. Y., Hamilton, M. F., Wilson, P. S. & Zabolotskaya, E. A. 2006 Bubble pulsations between parallel plates. *J. Accoust. Soc. Am.* **119** (4), 2067–2072.

Cunningham, K. B., Coleman, A. J., Leighton, T. G. & White, P. R. 2001 Characterising *in vivo* acoustic cavitation during lithotripsy with time-frequency methods. *Acoust. Bull.* **26** (5), 10–16.

Damianou, C. A., Sanghvi, N. T. & Fry, F. J. 1997 Dependence of ultrasonic attenuation and absorption in dog soft tissue on temperature and thermal dose. *J. Acoust. Soc. Am.* **102** (1), 628–634.

Dear, J. P. & Field, J. E. 1988 High-speed photography of surface geometry effects in liquid/solid impact. *J. Appl. Phys.* **63**, 1015–1021.

Dear, J. P., Field, J. E. & Walton, A. J. 1988 Gas compression and jet formation in cavities collapsed by a shock wave. *Nature* **332**, 505–508.

Delius, M. 2000 History of shock wave lithotripsy. In *Proceedings of the 15th International Symposium on Nonlinear Acoustics at the Turn of the Millenium*, vol. 524, pp. 23–32.

Delius, M. & Gambihler, S. 1992 Sonographic imaging of extracorporeal shock wave effects in the liver and gallbladder of dogs. *Digestion* **52**, 55–60.

DH 2004 In *The NHS Improvement Plan: Putting People at the Heart of Public Services*, p. 80. UK Dept. of Health Publication Cm 6268, 24 June 2004, Stationary Office, London.

Ding, Z. & Gracewski, S. M. 1996 The behaviour of a gas cavity impacted by a weak or strong shock wave. *J. Fluid Mech.* **309**, 183–209.

Duck, F. 2010 Tissue nonlinearity. *Proc. Inst. Mech. Engrs, Part H: J. Engng. in Med.* **224** (2), 155–170.

Eisenmenger, W. 2001 The mechanisms of stone fragmentation in ESWL. *Ultrasound Med. Biol.* **27** (5), 683–693.

Farassat, F. & Myers, M. K. 1988 Extension of Kirchhoff's formula to radiation from moving surfaces. *J. Sound Vib.* **123** (3), 451–461.

Farassat, F. & Succi, G. P. 1983 The prediction of helicopter descrete frequency noise. *Vertica* **7** (4), 309–320.

Fedele, F. 2008 Acoustic sensing of renal stones fragmentation in extracorporeal shockwave lithotripsy. PhD thesis, University of Southampton, UK.

Fedele, F., Coleman, A. J., White, P. R. & Hurrell, A. M. 2004 Development of a new diagnostic sensor for extra-corporeal shock-wave lithotripsy. Proceedings of the First Conference on Advanced Metrology for Ultrasound in Medicine. *J. Phys.: Conf. Ser.*, 134–139.

Fedele, F., Thomas, K., Leighton, T. G., Ryves, S., Phillips, D. & Coleman, A. J. 2010 A passive acoustic monitor of treatment effectiveness during extracorporeal lithotripsy. Proceedings of the Second Conference on Advanced Metrology for Ultrasound in Medicine. *J. Phys.: Conf. Ser*. **279**, 1–6.

Field, J. E. 1994 Experimental studies of bubble collapse. In *Bubble Dynamics and Interface Phenomena* (ed. J. R. Blake), pp. 17–31. Kluwer Academic.

Field, J. E., Swallowe, G. M. & Heavens, S. N. 1982 Ignition mechanisms of explosives during mechanical deformation. *Proc. R. Soc. Lond.* A **383**, 231–244.

Fong, S. W., Klaseboer, E., Turangan, C. K., Khoo, B. C. & Hung, K. C. 2006 Numerical analysis of a gas bubble near bio-materials in an ultrasound field. *Ultrasound Med. Biol.* **32**, 925–942.

di Francescantonio, P. 1997 A new boundary integral formulation for the prediction of sound radiation. *J. Sound Vib.* **202** (4), 491–509.

Freund, J. B. 2008 Suppression of shocked-bubble expansion due to tissue confinement with application to shock-wave lithotripsy. *J. Acoust. Soc. Am.* **123** (5), 2867–2874.

Gao, F. R., Hu, Y. T. & Hu, H. P. 2007 Asymmetrical oscillation of a bubble confined inside a micro pseudoelastic blood vessel and the corresponding vessel wall stresses. *Intl J. Solid Struct.* **44** (22–23), 7197–7212.

Gol'dberg 1956 Second approximation acoustic equations and the propagation of plane waves of finite amplitude. *Sov. Phys. Acoust.* **2**, 346–350.

Goss, S. A., Johnston, R. L. & Dunn, F. 1980 Compilation of empirical ultrasound properties of mammalian tissues. Part II. *J. Acoust. Soc. Am.* **68** (1), 93–108.

Hamilton, M. F. & Blackstock, D. T. 1998 In *Nonlinear Acoustics, Theory and Applications*, p. 102. Academic Press.

Haran, M. E. & Cook, B. D. 1983 Distortion of finite amplitude ultrasound in lossy media. *J. Acoust. Soc. Am.* **73**, 774–779.

Hirsimaki, H. M., Birkin, P. R., Frey, J. G. & Leighton, T. G. 2006 The laser-induced formation of plasma bubbles in water–electrochemical measurements. *Proc. Inst. Acoust.* **28** (1), 876–884.

Howell, B. P. & Ball, G. J. 2000 Damping of mesh-induced errors in free-Lagrange simulations of Richtmyer–Meshkov instability. *Shock Waves* **10**, 253–264.

Howell, B. P. & Ball, G. J. 2002 A free-Lagrange augmented Godunov method for the simulation of elastic–plastic solids. *J. Comput. Phys.* **175**, 128–167.

Iloreta, J. I., Fung, N. & Szeri, A. J. 2008 Dynamics of bubbles near a rigid surface subjected to a lithotripter shock wave. Part 1. Consequences of interference between incident and reflected waves. *J. Fluid Mech.* **616**, 43–61.

Jamaluddin, A. R. 2005 Free-Lagrange simulations of shock–bubble interaction in extracorporeal shock wave lithotripsy. PhD thesis, University of Southampton, U.K.

Jamaluddin, A. R., Ball, G. J. & Leighton, T. G. 2002 Free-Lagrange simulations of shock/bubble interaction in shock wave lithotripsy. In *Proceedings of the Second International Conference on Computational Fluid Dynamics (ICCFD)*, Sydney, Australia, pp. 541–546.

Jamaluddin, A. R., Ball, G. J. & Leighton, T. G. 2004 Free-Lagrange simulations of shock/bubble interaction in shock wave lithotripsy. In *Proceedings of the 24th International Symposium on Shock Waves,* Beijing, China, pp. 1211–1216.

Jarvinen, T. A., Jarvinen, T. L., Kaariainen, M., Kalimo, H. & Jarvinen, M. 2005 Muscle injuries: Biology and treatment. *Am. J. Sports Med.* **33** (5), 745–764.

Johnsen, E. & Colonius, T. 2009 Numerical simulations of non-spherical bubble collapse. *J. Fluid Mech.* **629**, 231–262.

Kendrinskii, V. K. 1997 The role of cavitation effects in the mechanisms of destruction and explosive process. *Shock Waves* **7**, 63–76.

Klaseboer, E., Fong, S. W., Turangan, C. K., Khoo, B. C., Szeri, A. J., Calvisi, M. L., Sankin, G. N. & Zhong, P. 2007 Interaction of lithotripter shockwaves with single inertial cavitation bubbles. *J. Fluid Mech.* **593**, 33–56.

Klaseboer, E., Turangan, C. K., Fong, S. W., Liu, T. G., Hung, K. C. & Khoo, B. C. 2006 Simulations of pressure–pulse bubble interaction using boundary element method. *Comput. Meth. Appl. Engng* **195**, 4287–4302.

Kornfeld, M. & Suvorov, L. 1944 On the destructive action of cavitation. *J. Appl. Phys.* **15**, 495–506.

Kuwahara, M., Ioritani, N., Kambe, K., Shirai, S., Taguchi, K., Saitoh, T., Orikasa, S., Takayama, K., Aida, S. & Iwama, N 1989 Hyperechoic region induced by focused shock waves *in vitro* and *in vivo*: Possibility of acoustic cavitation bubbles. *J. Lithotripsy Stone Dis.* **1**, 282–288.

Lauterborn, W. 1972 High-speed photography of laser-induced breakdown in liquids. *Appl. Phys. Lett.* **21**, 27.

Lauterborn, W. & Kurz, T. 2010 Physics of bubble oscillations. *Rep. Prog. Phys.* **73** (10), 106501.

Lea, S. C., Price, G. J. & Walmsley, A. D. 2005 A study to determine whether cavitation occurs around dental ultrasonic scaling instruments. *Ultrason. Chem.* **12** (3), 233–236.

Leighton, T. G. 1994 In *The Acoustic Bubble*. The Academic Press.

Leighton, T. G. 2004 From seas to surgeries, from babbling brooks to baby scans: The acoustics of gas bubbles in liquids. *Intl J. Mod. Phys.* B **18**, 3267–3314.

Leighton, T. G. 2007 What is ultrasound? *Prog. Biophys. Mol. Biol.* **93** (1–3), 3–83.

Leighton, T. G., Birkin, P. R., Hodnett, M., Zeqiri, B., Power, J. F., Price, G. J., Mason, T., Plattes, M., Dezkunov, N. & Coleman, A. J. 2005 Charaterisation of measures of reference acoustic cavitation (comorac): An experimental feasibility trial. In *Bubble and Particle Dynamics in Acoustic Fields: Modern Trends and Applications* (ed. A. A. Doinikov), pp. 37–94. Research Signpost.

Leighton, T. G. & Cleveland, R. O. 2010 Lithotripsy. In Proceedings of the Institute of Mechanical. Engrs, Part H. J. Engng. Med. **224** (2), 317–342.

Leighton, T. G., Cox, B. T. & Phelps, A. D. 2000 The Rayleigh-like collapse of a conical bubble. *J. Acoust. Soc. Am.* **107** (1), 130–142.

Leighton, T. G., Farhat, M., Field, J. E. & Avellan, F. 2003 Cavitation luminescence from flow over a hydrofoil in a cavitation tunnel. *J. Fluid Mech.* **480**, 43–60.

Leighton, T. G., Fedele, F., Coleman, A. J., McCarthy, C., Jamaluddin, A. R., Turangan, C. K., Ball, G. J., Ryves, S., Hurrell, A. M., Stefano, A. De & White, P. R. 2008*a* The development of a passive acoustic device for monitoring the effectiveness of shock wave lithotripsy in real time. *Hydroacoustics* **11**, 159–180.

Leighton, T. G., Fedele, F., Coleman, A. J., McCarthy, C., Ryves, S., Hurrell, A. M., Stefano, A. De & White, P. R. 2008*b* Clinical studies of a real-time monitoring of lithotripter performance using passive acoustic sensors. In *Proceedings of the Second International Urolithiasis Research Symposium*, Indianapolis, USA, pp. 256–277.

Leighton, T. G., Fedele, F., Coleman, A. J., McCarthy, C., Ryves, S., Hurrell, A. M., Stefano, A. De & White, P. R. 2008*c* A passive acoustic device for real-time monitoring the efficacy of shockwave lithotripsy treatment. *Ultrasound Med. Biol.* **34** (10), 1651–1665.

Leighton, T. G., Ho, W. L. & Flaxman, R. 1997 Sonoluminescence from the unstable collapse of a conical bubble. *Ultrasonics* **35**, 399–405.

Leighton, T. G., Phelps, A. D., Cox, B. T. & Ho, W. L. 1998 Theory and preliminary measurements of the Rayleigh-like collapse of a conical bubble. *Acustica with Acta Acustica* **84** (6), 1014–1024.

Leighton, T. G., White, P. R. & Marsden, M. A. 1995*a* Applications of one-dimensional bubbles to lithotripsy, and to diver response to low frequency sound. *Acta Acustica* **3**, 517–529.

Leighton, T. G., White, P. R. & Marsden, M. A. 1995*b* The one-dimensional bubble: An unusual oscillator, with applications to human bioeffects of underwater sound. *Eur. J. Phys.* **16**, 275–281.

Lindau, O. & Lauterborn, W. 2003 Cinematographic observation of the collapse and rebound of a laser-produced cavitation bubble near a wall. *J. Fluid Mech.* **479**, 327–348.

Lingeman, J. E., McAteer, J. A., Gnessin, E. & Evan, P. 2009 Shock wave lithotripsy: advances in technology and technique. *Nat. Rev. Urol.* **6**, 660–670.

Liu, X., Li, J., Gong, X. & Zhang, D. 2006 Nonlinear absorption in biological tissue for high intensity focused ultrasound. *Ultrasonics* **44**, e27–e30.

Lyrintzis, A. S. & George, A. R. 1989 Use of the Kirchhoff method in acoustics. *AIAA J.* **27** (10), 1451–1453.

Lyrintzis, A. S. & Xue, Y. 1991 Study of the noise mechanisms of transonic blade–vortex interactions. *AIAA J.* **29** (10), 1562–1572.

van der Meulen, J. H. J. 1986*a* On correlating erosion and luminescence from cavitation on a dydrofoil. In *Proceedings of the International Symposium on Propellers and Cavitation*, pp. 13–19.

van der Meulen, J. H. J. 1986*b* The relation between noise and luminescence from cavitation on a hydrofoil. In *Joint ACSE/ASME Conference on Cavitation in Hydraulic Structures and Turbomachinery* (ed. R. E. A. Arndt & D. R. Web), pp. 149–159.

O'Brien, W., Yang, Y. & Simpson, D. 2004 Evaluation of unscanned-mode soft-tissue thermal index for rectangular sources and proposed new indices. *Ultrasound Med. Biol.* **30** (7), 965–972.

Ohl, C. D., Kurz, T., Geisler, R., Lindau, O. & Lauterborn, W. 1999 Bubble dynamics, shock waves and sonoluminescence. *Phil. Trans. R. Soc. Lond.* A **357**, 269–294.

O'Leary, R., Sved, A. M., Davies, E. H., Leighton, T. G., Wilson, T. G. & Kieser, J. B. 1997 The bacterial effects of dental ultrasound on *Actinobacillus Actiomycetemcomitans* and *Porphyromonas Gingivalis* – an *in vitro* investigation. *J. Clin. Periodontol.* **24**, 432–439.

Philipp, A. & Lauterborn, W. 1998 Cavitation erosion by single laser-produced bubbles. *J. Fluid Mech.* **361**, 75–116.

Sankin, G. N., Simmons, W. N., Zhu, S. L. & Zhong, P. 2005 Shockwave interaction with laser generated single bubbles. *Phys. Rev. Lett.* **95**, 034501.

Sapozhnikov, O. A., Maxwell, A. D., MacConaghy, B. & Bailey, M. R. 2007 A mechanistic analysis of stone fracture in lithotripsy. *J. Acoust. Soc. Am.* **121**, 1190–1202.

Sassaroli, E. & Hynynen, K. 2007 Cavitation threshold of microbubbles in gel tunnels by focused ultrasound. *Ultrasound Med. Biol.* **33** (10), 1651–1660.

Shima, A. 1997 Studies of bubble dynamics. *Shock Waves* **7**, 33–42.

Smith, N. C., Fedele, F., Leighton, T. G., Coleman, A. J. & Thomas, K. 2009 The 'Smart Stethoscope': Predicting the outcome of lithotripsy Abstract. *BJU Intl (formerly: Br. J. Urol.)* **103** (4), pp. 32.

Takayama, K. 1999 Application of shock wave research to medicine. In *Proceedings of the 22nd International Symposium on Shock Waves*, London, UK, pp. 23–32.

Tomita, Y. & Shima, A. 1986 Mechanisms of impulsive pressure generation and damage pit formation by bubble collapse. *J. Fluid Mech.* **169**, 535–564.

Tong, R. P., Schiffers, W. P., Shaw, S. J., Blake, J. R. & Emmony, D. C. 1999 The role of 'splashing' in the collapse of a laser-generated cavity near a rigid boundary. *J. Fluid Mech.* **380**, 339–361.

Turangan, C. K. 2004 Free-Lagrange simulations of cavitation bubble collapse. PhD thesis, University of Southampton, U.K.

Turangan, C. K., Jamaluddin, A. R., Ball, G. J. & Leighton, T. G. 2008 Free-Lagrange simulations of the expansion and jetting collapse of air bubbles in water. *J. Fluid Mech.* **598**, 1–25.

Turangan, C. K., Ong, G. P., Klaseboer, E. & Khoo, B. C. 2006 Experimental and numerical study of transient bubble–elastic membrane interaction. *J. Appl. Phys.* **100**, 054910.

Vian, C. J. B., Birkin, P. R. & Leighton, T. G. 2010 Cluster collapse in a cylindrical cell: Correlating multibubble sonoluminescence, acoustic pressure and erosion. *J. Phys. Chem.* C **114** (39), 16416–16425.

Vogel, A., Lauterborn, W. & Timm, R. 1989 Optical and acoustic investigations of the dynamics of laser-produced cavitation bubbles near a solid boundary. *J. Fluid Mech.* **206**, 299–338.

Whittingham, T. 2007 Wfumb safety symposium on echo-contrast agents: Exposure from diagnostic ultrasound equipment relating to cavitation risk. *Ultrasound Med. Biol.* **33** (2), 214–223.

Zderic, V., Keshavarzi, A., Andrew, M. A., Vaezy, S. & Martini, R. W. 2004 Attenuation of porcine tissues *in vivo* after high intensity ultrasound treatment. *Ultrasound Med. Biol.* **30** (1), 61–66.

Zequiri, B., Hodnett, M. & Leighton, T. G. 1997 A strategy for the development and standardisation of measurement methods for high power/cavitating ultrasound fields – final project report. *Tech. Rep.*, NPL Rep. CIRA(EXT)016.

Zhong, P., Cioanta, I., Cocks, F. H. & Preminger, G. M. 1997 Inertial cavitation and associated acoustic emission produced during electrohydraulic shock wave lithotripsy. *J. Acoust. Soc. Am.* **101** (5 Pt 1), 2940–2950.

Zhong, P., Zhou, Y. & Zhu, S. 2001 Dynamics of bubble oscillations in constrained media and mechanisms of vessel rupture in swl. *Ultrasound Med. Biol.* **27**, 119–134.

Zhu, S. L., Cocks, F. H., Preminger, G. M. & Zhong, P. 2002 The role of stress waves and cavitation in stone comminution in shock wave lithotripsy. *Ultrasound Med. Biol.* **27**, 661–671.